TECHNISCHE UNIVERSITÄT MÜNCHEN

Department Chemie

Lehrstuhl für Theoretische Chemie

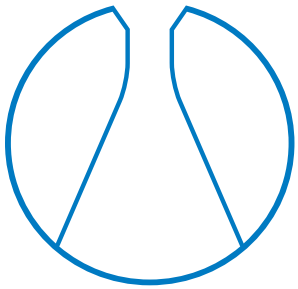

Shape and Catalytic Mechanism of RuO_2 Particles at CO Oxidation Reaction Conditions:

First-Principles Based Multi-Scale Modeling

DISSERTATION

Tongyu Wang

TECHNISCHE UNIVERSITÄT MÜNCHEN

Lehrstuhl für Theoretische Chemie

Shape and Catalytic Mechanism of RuO_2 Particles at CO Oxidation Reaction Conditions: First-Principles Based Multi-Scale Modeling

Tongyu Wang

Vollständiger Abdruck der von der Fakultät für Chemie der Technischen Universität München zur Erlangung des akademischen Grades eines

Doktor der Naturwissenschaften (Dr. rer. nat)

genehmigten Dissertation.

Vorsitzender: Univ.-Prof. Dr. Ville Kaila

Prüfer der Dissertation:

1. Univ.-Prof. Dr. Karsten Reuter
2. Univ.-Prof. Dr. Sebastian Günther

Die Dissertation wurde am 17.09.2015 bei der Technischen Universität München eingereicht und durch die Fakultät für Chemie am 14.10.2015 angenommen.

Abstract

A central objective of heterogeneous catalysis research is to establish structure-morphology-activity relationships. However, due to experimental difficulties in determining the crystal habit under reaction conditions, such relationships are yet scarcely built up. The hitherto primarily feasible access are so-called ex-situ studies, which neglect the attested possibly strong dynamical evolution of operating catalysts and the significant effect that this can have on the catalytic function. In this situation, independent information from first-principles-based theory can be an enormous asset.

This route is pursued in this thesis, and CO oxidation on RuO_2 nanoparticles is chosen as a prototypical system. The hitherto almost exclusively studied lowest-energy RuO_2(110) facet was recently shown to deactivate into a RuO_2(100)-c(2x2) structure under O-rich reaction conditions. In contrast, increasing activity of the nanoparticles upon changing to more reducing conditions has been reported. This could be due to the stabilization of an O-deficient RuO_2 terminations or the evolution to a different crystal shape while on stream. To scrutinize the latter hypothesis, the surface structure and composition of low-index RuO_2 facets at different oxidation conditions is first investigated using density-functional theory (DFT) calculations combined within *ab initio* thermodynamics. The resulting DFT-based Wulff construction of the equilibrium shape of RuO_2 particles in an oxygen environment allows for a detailed discussion of the dependence of the oxidizing pretreatment used in recent powder catalyst studies. The analysis specifically indicates an incomplete particle shape equilibration in previously used low temperature calcination. We suggest that the equilibrated particles could be active CO oxidation catalysts with long-term stability in oxidizing feed and then represent an interesting alternative to a previously suggested the core-shell concept.

Moreover, the obtained results point at a prominent role of the hitherto little studied apical facets for the long-term catalytic activity. To scrutinize this we perform DFT-based kinetic Monte Carlo simulations of CO oxidation at the (111) facet of RuO_2. Comparing the detailed insight into elementary processes, steady-state surface coverages and catalytic activity to equivalent published simulation data for the frequently studied RuO_2(110) facet, qualitative differences are identified in virtually every aspect ranging from binding energetics over lateral interactions to the interplay of elementary processes at the different active sites. Nevertheless, particularly at

technologically relevant elevated temperatures, near-ambient pressures and near-stoichiometric feeds both facets exhibit almost identical catalytic activity. This can be an important aspect in understanding the long-term steady-state activity of RuO_2 nanoparticles observed in experiments. Furthermore, these findings challenge the traditional definition of structure sensitivity based on macroscopically observable turnover frequencies, in which the role of electronic effects due to a different degree of under-coordination of surface atoms, as well as the role of geometric effects due to different bonding configurations are considered as the most important factors for metal catalysts. For oxide surface our study suggests that the spatial distribution of the active sites and concomitant diffusion limitations constitute a third important factor.

Our theoretical study on RuO_2 polycrystalline powders builds up an appealing link between detailed surface science work on single crystals and the supported nanoparticles in real catalysis. This ansatz offers a general route to the exploration of important factors such as particle size, shape, composition and catalytic activity without the additional complexity introduced by a support material. Our work thus serves as an important step along the long-term track of systematically bridging between single-crystal model and real catalysis.

Zusammenfassung

Eine der Hauptaufgaben in der Forschung über heterogene Katalyse ist es das Verhältnis zwischen der Struktur, Morphologie und Aktivität von Katalysatorpartikeln zu etablieren. Bislang sind solche Korrelationen kaum erarbeitet, unter anderem auch durch experimentelle Limitierungen die Kristallform unter laufenden Reaktionsbedingungen zu bestimmen. Primär kann dies bisher nur in sogenannten ex-situ Untersuchungen erfolgen, die aber eine eventuell starke dynamische Veränderung aktiver Katalysatoren unter Reaktionsbedingungen nicht berücksichtigen. In dieser Situation birgt die unabhängige Information von ab initio basierter Theorie und Modellierung ein enormes Potenzial.

Dieser Ansatz wird in dieser Arbeit verfolgt. Speziell wird die CO Oxidation an RuO_2 Nanoteilchen als ein prototypisches Modellsystem gewählt. Neuere Arbeiten zeigen eine Deaktivierung der erschöpfend untersuchten, niederenergetischen RuO_2(110) Facette unter Sauerstoff-reichen Reaktionsbedingungen durch Mikrofacettierung in eine RuO_2(100)-c(2x2) Struktur. Im Gegensatz hierzu wurde eine zunehmende Aktivität der RuO_2 Nanoteilchen unter reduzierenden Reaktionsbedingungen beobachtet. Dies könnte auf eine Stabilisierung O-defizienter RuO_2 Terminierungen oder eine dynamische Veränderung der Kristallform zurückgeführt werden. Um diese Hypothesen zu prüfen wird die Oberflächenstruktur und die Zusammensetzung aller niedrig-indizierten RuO_2 Facetten in unterschiedlichen Oxidationsbedingungen zunächst mit Hilfe der Dichtefunktionaltheorie (DFT) in Kombination mit thermodynamischen Methoden untersucht. Die resultierende DFT-basierte Wulff Konstruktion der Gleichgewichtsform von RuO_2 Teilchen in einer Sauerstoffumgebung ermöglicht eine detaillierte Diskussion über die Abhängigkeit der oxidativen Vorbehandlung in zuletzt durchgeführten experimentellen Arbeiten an polykristallinen Pulvern. Die Analyse deutet insbesondere auf eine unvollständige Equilibrierung der Teilchenform bei der teilweise verwendeten Kalzinierung bei niedriger Temperatur. Equilibrierte Teilchen könnten hingegen aktive CO Oxidationskatalysatoren mit langfristiger Stabilität unter Sauerstoff-reichen Bedingungen sein und dann eine interessante Alternative zum bisher vorgeschlagenen Core-Shell Konzept darstellen.

Darüber hinaus deuten die Ergebnisse eine wichtige Rolle der bisher wenig untersuchten apikalen Facetten für die langfristige katalytische Aktivität an. Um dies zu

untersuchen führen wir eine DFT-basierte kinetische Monte-Carlo-Studie zur CO-Oxidation an der (111) Facette von RuO_2 durch. Im detaillierten Vergleich der Elementarprozesse, der Bedeckungen im stationären Zustand, und der katalytische Aktivität mit früher veröffentlichten Simulationsdaten für die extensiv untersuchte RuO_2(110) Facette zeigen sich qualitative Unterschiede in praktisch jedem Aspekt von Bindungsenergien über laterale Wechselwirkungen bis hin zum Zusammenspiel der elementaren Prozesse an den verschiedenen aktiven Zentren. Dennoch weisen beide Facetten fast identische katalytische Aktivität auf, vor allem bei technisch-relevanten erhöhten Temperaturen, bei (fast) atmosphärischen Drücken und grob stöchiometrischen Partialdrücken. Dieser Umstand könnte ein grundlegendes Puzzlestück zum Verständnis der experimentell beobachteten Langzeit-Aktivität von RuO_2 Partikeln sein. Darüber hinaus sind diese Ergebnisse im Hinblick auf die traditionelle Definition einer Struktursensitivität interessant, die allein auf makroskopisch beobachtbaren Umsatzfrequenzen basiert. Bisher werden hierfür elektronische Effekte aufgrund einer unterschiedlichen Unterkoordinierung der Oberflächenatome, sowie geometrische Effekte aufgrund der unterschiedlichen Bindungskonfigurationen als die wichtigsten Faktoren für Metallkatalysatoren betrachtet. Für Oxide weist unsere Studie auf einen dritten wichtigen Faktor in Form der räumliche Verteilung der aktiven Stellen bei gleichzeitigen Diffusionsbeschränkungen hin.

Unsere theoretische Untersuchung zu polykristallinen RuO_2 Pulvern errichtet eine zukunftsweisende Verbindung zwischen detaillierten Studien im Surface Science Kontext an Einkristallen und den geträgerten Nanopartikeln in der realen Katalyse. Dieser Ansatz bietet einen allgemeinen Weg zur Erforschung von Faktoren wie Teilchengröße, Form, Zusammensetzung und katalytischer Aktivität, ohne die durch ein Trägermaterial zusätzlich eingeführte Komplexität. Unsere Arbeit dient somit als einen wichtiger Schritt in Richtung der langfristig verfolgten systematischen Brückenbildung zwischen Einkristall-Modellkatalysatoren und realer Katalyse.

Contents

1

Introduction

1.1 Scientific background

Gasoline-engine exhaust, especially CO, is a serious threat to the environment and public health, so environmentally benign technologies are required to eliminate this poisonous gas. An efficient way of removing CO is catalytic oxidation of CO to CO_2. Although this reaction has been an extensively studied model in heterogeneous catalysis research for many decades, increasing atomic-scale characterization and understanding in recent years reveals an unexpected complexity that is now strongly debated in the literature.[1-4] Much of this debate concerns the oxidization of the predominantly employed late transition metal catalysts[5-7] in the O-rich environments under near-ambient technological operation. The really active state of the working catalyst is not the metal in its original state, but possibly a formed bulk oxide, or an oxidized film of a core-shell structured nanoparticle.[8-11]

CO oxidation at Ru catalysts has been high up on the research agenda of oxide formation due to an enigmatic huge activity difference of Ru. This particular system has the lowest reactivity in ultra-high vacuum (UHV), while shows the highest reactivity under near-ambient conditions.[5, 7, 11-13] Particular interest in CO oxidation over Ru was originally triggered by Cant, Hicks and Lennon[7] working on supported catalysts. Under UHV conditions their Ru catalyst exhibited by far the lowest activity among the studied late transition metals, while under reactant pressures of atmospheres, the situation was reversed, and a superior activity of Ru compared to Pt, Rh or Pd was measured. Practically identical activities also for the Ru(0001) single crystal surface were subsequently obtained by Peden and Goodman,[4] which motivated an almost complete focus on this particular surface for many years thereafter. The enigmatic difference was rationalized by the characterization of a thin RuO_2(110) film formed during the CO oxidation, i.e. it was attributed to oxide formation. In other words, the pristine Ru metal present in UHV is a bad catalyst, while at near-ambient conditions it transforms into active RuO_2.[10-11, 14] Subsequent research predominantly focused on the dominant facet Ru(0001) of Ru particles and the RuO_2(110) orientation which forms on top of it. These studies included a wealth of atomic-scale in-situ characterization techniques,[8, 15] as well as refined first-principles modelling that culminated in a complete microkinetic description of the steady-state catalytic activity of RuO_2(110).[13, 16-18]

However, this view of the oxide,[1-4, 19] particularly of the coordinatively unsaturated sites at $RuO_2(110)$[7,20-21] as the most active state in the CO oxidation, has recently been increasingly challenged. While Goodman and coworkers favour the activity of a fully O covered Ru(0001) surface,[1] Böttcher et al.[10, 15] introduced a model including subsurface oxygen dissolved in Ru. Although dedicated in-situ characterization techniques such as in-situ X-ray diffraction (XRD),[19] in-situ surface XRD,[8] in-situ X-ray photoelectron spectroscopy (XPS) and in-situ polarization modulation infrared reflection absorption spectroscopy (PM-IRAS)[22] have been increasingly applied, no fully conclusive atomic-scale evidence in favour or against either of the three conceptions – bulk oxide, metal or transient surface oxide – has yet been established. What seems rather clear is that the hitherto prominently studied $RuO_2(110)$ facet deactivates, presumably due to micro-facetting into a $RuO_2(100)$-c(2x2) structure.[9, 23-24] This would also rationalize the observation of an irregular octagonal cross section habit of calcined RuO_2 crystals compared to the obelisk-like habit as resulting from dominant lowest-energy $RuO_2(110)$ facets.[25] The activity seems also closely related to the employed gas-phase conditions. Wakita et al.,[20] Cant et al.[7] and Kiss and Gonzalez[21] found the deactivation of supported Ru catalysts under O_2-rich reaction conditions. While such deactivation has sometimes been related to an inactivity of fully oxidized RuO_2 per se, it could also arise from the stabilization of a specific O-rich termination on an otherwise active facet or a crystal shape change adapting to the O-rich feed. Similarly, the observed increasing activity upon changing to more reducing conditions has sometimes been ascribed to a higher activity of a metallic Ru state, but could also arise out of the stabilization of an O-deficient RuO_2 termination or a different crystal shape. Specifically, the work by Rosenthal et al. favours active sites on the hitherto only scarcely studied (101) and (111) surfaces, and their detailed transmission electron microscopy data of the behaviour of RuO_2 crystals provides stringent boundaries for the surface free energies of the yet unknown most stable structures of these two facets.

While a highly active state of heavily reduced, presumably metallic Ru has recently been unequivocally established by Rosenthal et al.,[22] this still calls for a detailed investigation of the surface structure and composition of low-index RuO_2 facets at different CO oxidation reaction conditions in a wide scope away from the experimental studies as well as the corresponding catalytic mechanism. To predict these materials

properties, a consistent treatment in the wide hierarchy of scales from the electronic level to macroscopic lengths and times is required.

Within the electronic level, density-functional theory (DFT)[26-28] is a quantum mechanical theory which has matured to a standard tool to simulate elementary processes in the micro-scale regime. The principle of DFT is that the ground state of a system is only dependent on the electron density of the system. From this density the total energy of the system and the forces on the atoms can be calculated. With this information, other properties of the potential energy surface (PES), such as the relaxed atomic geometry (local PES minima) or the vibrational modes (curvature around the PES minima) can be accessed. The treatment of electronic exchange and correlation is the main source of uncertainty in practical DFT calculations. Presently, approximate exchange-correlation functionals based on the generalized gradient approximation (GGA)[29-31] are the common workhorse for large-scale calculations of extended (metallic) systems.

A straightforward way to connect DFT electronic structure calculations to macroscopic system properties at finite temperature and pressure is to use the energetic and vibrational data in the calculation of thermodynamic potentials. In the application of this approach, often termed '*ab initio* (atomistic) thermodynamics' for surfaces exposed to realistic gas-phases, the central target quantity is the surface free energy, which is minimized by the most stable structure[24]. Computing the surface free energy for a range of candidate structures in equilibrium with appropriate bulk and gas-phase reservoirs allows to conclude on the stability, albeit always with the limitation that this conclusion only extends to the compared pool of structures. Combining obtained insight for various low-index surfaces into a classical Wulff construction extends this approach to the equilibrium crystal shape in the considered environment. This includes in an approximate way also multi-component gas-phases characteristic for heterogeneous catalysis, if the corresponding different gas-phase reservoirs are treated separately in 'constrained' equilibrium with the surface.[32-33]

More accurate insight into the surface structure and function in the catalytic application requires a shift to explicit kinetic theories, e.g. the kinetic Monte Carlo approach[34-35] or mean-field based micro-kinetic formulations.[36-37] Central ingredients to such approaches are the kinetic rate constants of the individual elementary processes. Within reaction

rate theories, like harmonic transition state theory,[38-40] these rate constants are related to PES properties accessible to DFT. This concerns in particular the barrier for the transition state. A common way to determine the saddle point and connected minimum energy path between known reactant and product states is the nudged elastic band (NEB) method.[41-42] The method works by optimizing a number of intermediate images along the reaction path. Each image finds the lowest energy possible while maintaining equal spacing to neighbouring images. Due to this spacing, in most cases the searched saddle point (transition state) is not the real saddle point. To overcome this shortcoming, the NEB method is improved to the climbing image NEB method (CI-NEB).[43]

With the above multi-scale modelling methods, the shape and catalytic mechanism of RuO_2 particles at CO oxidation reaction conditions will be studied.

1.2 Outline

This thesis is structured as follows:

We first provide an overview of the fundamental theoretical concepts that this work is based on. We start with an accurate analytic description of the many-electron problem, and then discuss Hartree-Fock and density functional theory (DFT) as approximate but numerically feasible methods to resolve the electronic structure. For the determination of the kinetic rate constants from first-principles, we describe the drag method and climbing image NEB method (CI-NEB) which are used for the determination of the barrier for the transition state. Then we connect DFT electronic structure calculations to mesoscopic system properties at finite temperature and pressure with '*ab initio* (atomistic) thermodynamics'. This is followed by a discussion of the kinetic Monte Carlo approach for a more accurate insight into the surface structure and function in the catalytic application.

On the basis of this methodology we first employ *ab initio* thermodynamics methods to address the surface structure and composition of different RuO_2 low-index facets at different CO oxidation reaction conditions. The surface free energies of different facets as a function of the chemical potentials in the environment will be the input to a classical

Wulff construction, thereby providing first insight into the crystal shape of RuO_2 in gas-phases characteristic of CO oxidation conditions.

Based on the suggestions from the Wulff construction study with respect to possibly reactive facets other than the extensively studied RuO_2(110) facets, we present a first-principles kinetic Monte Carlo study of CO oxidation at the RuO_2(111) facet and establish a structure-reactivity relationship by detailed comparison of site arrangement, interplay of elementary processes and even the underlying individual elementary processes with that on RuO_2(110). This comparison sheds lights on the structure sensitivity classifications of metals and their corresponding transformation into structurally more complex oxides.

Finally we summarize our findings and discuss the ensuing work along our long-term track of systematically bridging between single-crystal model and real catalysis.

I. Theoretical background

Computational methods are becoming key contributors in the study of materials science, allowing to predict material properties or system behavior across all relevant length and time scales (see Fig. 2.1). So-called multi-scale modeling combines the separate insight from techniques at different scales and enables a rational design of novel catalysts and improvement of reactor design at operating conditions. Starting from the molecular level, first-principles electronic-structure calculations unravel bond making and breaking. At the mesoscopic scale, the interplay between all elementary processes in a catalytic cycle is simulated using statistical methods. The next level reaches the macroscopic scale, which accounts for heat and mass transfer effects in heterogeneous catalysis, e.g., through computational fluid dynamics.

In the following chapters, we will introduce the simulation approaches we are using for our research. In Chapter 2, we will describe electronic structure theory with a particular focus on density-functional theory as well as methods for locating transition states, which are employed to accurately describe all relevant molecular processes, including adsorption and desorption of reactants and products, as well as the surface chemical reactions. Based on corresponding knowledge of the atomistic structure and the properties of the individual elementary processes, we explore the mesoscopic regime using *ab initio* atomistic thermodynamics approaches and first-principles kinetic Monte Carlo simulations. In Chapter 3, we first introduce *ab initio* atomistic thermodynamics approaches which provide first insight into the composition and structure of the catalyst surface in reactive environments ranging from ultra-high vacuum to technologically relevant conditions with pressures of the order of atmospheres and elevated temperatures.[44] For a detailed study of the catalytic activity, we not only care about the surface configuration and composition under given conditions, but also put emphasis on how the chemical reactions take place on this surface. First-principles kinetic Monte Carlo simulations can answer the latter question by exploring the full dynamics of the system from picoseconds up to seconds, explicitly considering the detailed correlations, fluctuations and spatial distributions of the chemicals at the catalyst surface.[45]

2

Multi-scale modeling methods in electronic regime

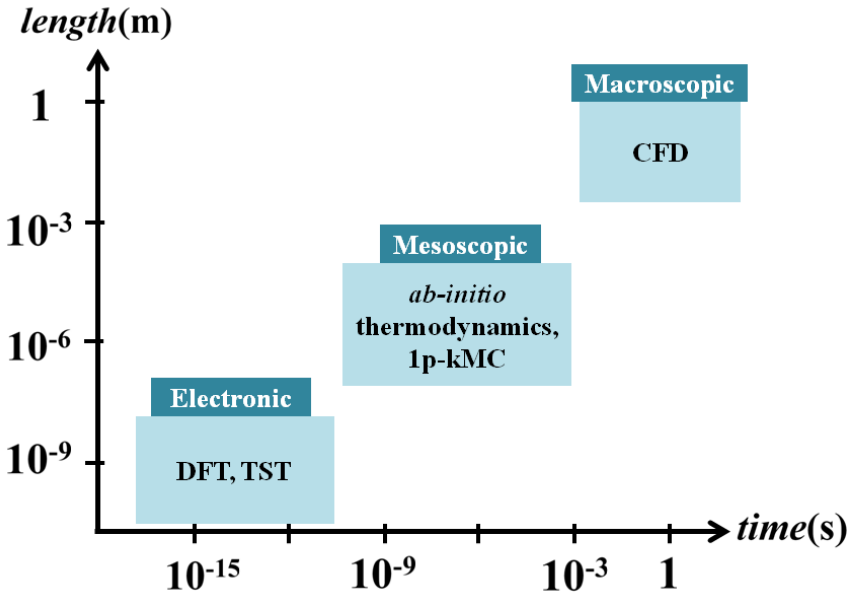

Figure 2.1 Regimes in time and length scale of multi-scale modeling methods in catalysis research.

This chapter will focus on the theory and methods at the lowest level, the electronic regime, as shown in Fig. 2.1.

2.1 Electronic structure theory

In the present context, electrons and nuclei are the fundamental particles, constituting atoms, molecules and condensed matter. Their stationary states are described by the famous time-independent non-relativistic Schrödinger equation[46]

$$\hat{H}\left|\Phi_i\right\rangle = E_i\left|\Phi_i\right\rangle \tag{2.1}$$

where $\hat{H}$ is the time-independent Hamilton operator. The eigenspectrum of the Hamiltonian contains all possible pure states $\left|\Phi_i\right\rangle$ of the system. The Hamiltonian corresponding to the many-body Schrödinger equation can be written as:

$$\hat{H} = \sum_i \frac{-\hbar^2\nabla_i^2}{2m_e} + \sum_I \frac{-\hbar^2\nabla_I^2}{2M_I} + \sum_{i,I} \frac{-Z_I e}{\left|r_i - R_I\right|} + \sum_{i,j} \frac{e^2}{\left|r_i - r_j\right|} + \sum_{I,J} \frac{Z_I Z_J}{\left|R_I - R_J\right|} \tag{2.2}$$

Here electrons with mass m_e are denoted by lower case subscripts and symbols, while nuclei with proton number Z_I and mass M_I are indicated by upper case ones. The terms on the right side of the equation represent the kinetic energy operator for electrons $\hat{T}_e$, the kinetic energy operator for the nuclei $\hat{T}_N$, the Coulomb potential between electrons and nuclei $\hat{V}_{eN}$, Coulomb potential between electrons $\hat{V}_{ee}$, and the Coulomb potential between nuclei $\hat{V}_{NN}$ respectively.

However, when more than one electron is involved, an analytic solution to this equation is inaccessible. This is because the Schrödinger equation is defined on a $3(N_e + N_N)$-dimensional domain, in which N_e is the number of electrons and N_N is the number of nucleus. Therefore approximate methods for solving the Schrödinger equation are necessary.

2.1.1 Adiabatic Born-Oppenheimer approximation

The first approximation arises from a separation of mass and time scales, called the adiabatic Born-Oppenheimer approximation[47]. The key idea comes from the fact that nuclei are approximately 1800 times heavier than electrons. Thus the inverse mass of a nucleus $1/M_I$ is rather small compared to that of electrons. If the approximation of the nuclear mass being infinity is made, their corresponding kinetic energy can be ignored. This allows to separate the total many-body wavefunction

$$|\Phi\rangle = |\Psi(R,r)\rangle|\Pi(R,t)\rangle \tag{2.3}$$

into the electronic wavefuction $|\Psi(R,r)\rangle$ and nuclear wavefunction $|\Pi(R,t)\rangle$. Both wavefunctions depend on the nuclear coordinates R, while the former one further depends on the electronic degrees of freedom r, and the later one further depends on the time t. From this ansatz, an effective Schrödinger equation for the electronic wave function can be derived by neglecting the coupling between the electronic and the nuclear wave functions. Thus the electronic Schrödinger equation can be solved independently for each configuration of the nuclei. The corresponding electronic Hamiltonian can be written as

$$\hat{H}_e = \hat{T}_e + \hat{V}_{ee} + \hat{V}_{eN} \tag{2.4}$$

The above approximation that the electrons instantaneously adapt to a given configuration of nuclei is valid in many cases, except for some interesting physical effects like electron-phonon interaction, BCS theory of superconductivity or proton-tunneling, which require explicit treatment of the nuclear quantum effects, e.g. in a perturbative fashion. For the chemical applications we are studying in this thesis, using the above approximation helps us focus on the Hamiltonian for the electrons by treating the nuclear positions as parameters, thus the electronic Schrödinger equation can be solved independently for each configuration of nuclei.

2.1.2 Direct solution of the electronic Schrödinger equation

Plugging the above electronic Hamiltonian Eq. (2.4) into the Schrödinger equation Eq. (2.1), the fundamental equation for electronic structure theory is formulated.

$$\hat{H}\left|\Psi_i\left(\{r_i\}\right)\right\rangle = E_i\left|\Psi_i\left(\{r_i\}\right)\right\rangle \tag{2.5}$$

The direct solution of this electronic Schrödinger equation is a closed expression for the many-body wavefunction $\left|\Psi_i\left(\{r_i\}\right)\right\rangle$. However, it is still difficult to obtain. First, the electrons are explicitly correlated through the electron-electron Coulomb interaction $\hat{V}_{ee}$, which means that if the state or position of one electron changes, all other electrons will be affected; Secondly, electrons are fermions which are indistinguishable and obey Pauli's exclusion principle. This requires $\left|\Psi_i\left(\{r_i\}\right)\right\rangle$ to be anti-symmetric with respect to particle exchange

$$\left|\Psi_i\left(r_1, r_2, r_3, ..r_n\right)\right\rangle = -\left|\Psi_i\left(r_2, r_1, r_3, ..r_n\right)\right\rangle \tag{2.6}$$

Furthermore, $\left|\Psi_i\left(\{r_i\}\right)\right\rangle$ is a full *3n* dimensional sets, with *n* being the number of electrons. In this regard, even for a single oxygen atom with only 8 electrons and quite sparse grid (i.e., 10 grid points per dimension), storing the many-body wavefunctions would require storage of $10^{3\times 8}$ floating point numbers. This exceeds any computational resources in terms of memory demand. As a result, directly solving the many-body Schrödinger equation is not possible, although it contains the full information of the system.

2.1.3 Hartree-Fock approximation

One of the approaches to solving the many-body Schrödinger equation is the Hartree-Fock approximation, which was developed by D. R. Hartree and V. Fock[48-49]. This approach rephrases the correlated many-electron problem as a system of non-interacting electrons moving in an averaged Coulomb potential. The electronic exchange can be exactly accounted for through an anti-symmetric many-body wavefunction constructed from the single-particle orbitals. The base concept on which this approach rests builds a foundation for most modern quantum chemical methods.

In the many-body Hamiltonian, if the electron-electron interaction $\hat{V}_{ee}$ is treated as a system of non-interacting electrons moving in an averaged Coulomb potential, a single-particle spectrum of eigenstates $\{\phi_i\}$ with eigenvalues ε_i for the non-interacting electron can be expressed. Here, $\phi_i(r_j,\sigma_j)$ are spin-orbitals, formed with the position function $\varphi_i^{\sigma_j}(r_j)$ and the spin variable function $\alpha_i(\sigma_j)$. A many-body wavefunction should obey Pauli's principle, and the simplest form of it is the Slater determinant:[50]

$$\Psi = \frac{1}{\sqrt{n!}} \begin{vmatrix} \phi_1(r_1,\sigma_1) & \phi_2(r_1,\sigma_1) & \dots & \phi_n(r_1,\sigma_1) \\ \phi_1(r_2,\sigma_2) & \phi_2(r_2,\sigma_2) & \dots & \phi_n(r_2,\sigma_2) \\ \vdots & \vdots & & \vdots \\ \phi_1(r_n,\sigma_n) & \phi_2(r_n,\sigma_n) & \dots & \phi_n(r_n,\sigma_n) \end{vmatrix} \tag{2.7}$$

The corresponding Schrödinger-like differential-integral equations are the so-called Hartree-Fock equations:

$$\left[-\frac{1}{2}\nabla^2 + V_{eN}(r) + \sum_{j,\sigma_j} \int dr' \frac{\left|\varphi_j^{\sigma_j}(r')\right|^2}{|r-r'|} - \sum_j \int dr' \frac{\varphi_i^{\sigma_i}(r')\varphi_j^{\sigma_{j^*}}(r')}{|r-r'|} \right] \varphi_i^{\sigma}(r) = \varepsilon_i^{\sigma}\varphi_i^{\sigma}(r) \tag{2.8}$$

These equations constitute a coupled, non-linear set of differential equations that needs to be solved iteratively. The solutions φ_i^{σ} of this set of equations define states of quasi-independent electrons moving in a mean effective potential.

The Hartree-Fock approximation incorporates electronic exchange in an exact way through the ansatz of Slater determinants. However, this explicit electron-electron correlation is insufficient because it is only incorporated through the mean effective potential, stemming from the fact that the many-body wavefunction is approximated

through a single Slater-determinant. To cure the insufficient correlation effects, several strategies have been proposed, including a perturbative treatment (Møller-Plesset theory) and systematic expansions of the many-body wavefunction in a basis of many Slater- determinants.

2.2 Density-functional theory

2.2.1 Thomas-Fermi model

One year after Schrödinger's famous equation had been published, Thomas[26] and Fermi[51] developed a different approach to describing the electronic structure of condensed matter, which is not based on explicit wavefunctions but on the electronic density. In this approach, the electronic density is expressed as:

$$\rho(r) = n\int dr_2^3 ..dr_n^3 \left|\Psi(r_1, r_2, r_3 ..r_n)\right|^2 \tag{2.9}$$

The total energy can then be calculated as:

$$E_{DFT}[\rho] = T[\rho] + \int d^3 r \hat{V}_{eN}(r)\rho(r) + \int d^3 r d^3 r' \frac{\rho(r)\rho(r')}{|r - r'|} \tag{2.10}$$

The crucial advantage of this approach is to largely reduce the dimensionality of the problem. Instead of dealing with the *3n*-dimensional function $\left|\Psi_i\left(\{r_i\}\right)\right\rangle$, one only deals with the 3-dimensional function $\rho(r)$. However, the Thomas-Fermi approximation completely neglects exchange and correlation between electrons, thus it cannot even reproduce the chemical binding of molecules.[52] Nevertheless, this work by Thomas and Fermi is considered a milestone in electronic structure theory, providing the conceptual roots for DFT.

2.2.2 Hohenberg–Kohn theorems

DFT is one of the most popular and successful quantum mechanical approaches for the solution of many-body problems, allowing to calculate atomic ground state energies and observables including bond-lengths, bond-angles and binding energies of molecules and condensed matter.[53-54]

DFT was put on a firm theoretical footing by the two Hohenberg–Kohn theorems (HK

theorems).[55] The first H-K theorem demonstrates that the ground-state electronic density $\rho_0(r)$ unequivocally determines the external potential $\hat{V}_{eN}$ up to an additive constant, and thus determines the ground state many-body wavefunctions $\Psi_0(\{r_i\})$. This theorem is illustrated in Fig. 2.2. As a result, all ground state observables

$$\hat{O}_0 = \langle \Psi_0(\{r_i\}) | \hat{O} | \Psi_0(\{r_i\}) \rangle = \langle \Psi[\rho_0] | \hat{O} | \Psi[\rho_0] \rangle \tag{2.11}$$

are accessible through the ground state density. This theorem can be extended to the time-dependent domain to develop time-dependent density functional theory (TDDFT),[56] which can be used to describe excited states.

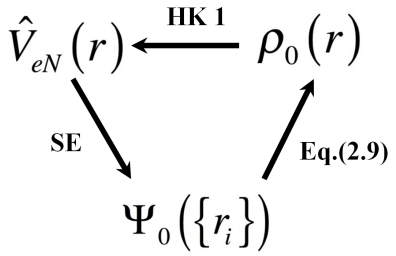

Figure 2.2 Illustration of the first Hohenberg-Kohn theorem (denoted as HK1). The external potential $\hat{V}_{eN}$ determines the ground-state many-body wavefunctions $\Psi_0(\{r_i\})$ through the Schrödinger equation (denoted as SE), while $\Psi_0(\{r_i\})$ defines the ground-state electronic density $\rho_0(r)$ through Eq. (2.9). $\rho_0(r)$ in turn determines the external potential $\hat{V}_{eN}$ up to an additive constant according to the first Hohenberg-Kohn theorem.

The second HK theorem[57-58] proves the existence of an energy expression as a universal functional of the electron density, the minimum of which yields the ground state density.

2.2.3 Kohn-Sham density-functional theory

DFT became the most widely used method for electronic structure calculations after the pioneering work by Kohn and Sham.[59] Kohn-Sham DFT reduces the intractable many-body problem of interacting electrons in a static external potential to a tractable problem of non-interacting electrons moving in an effective potential, thus making the solution for many-body systems computational cheap and accessible.

Kohn-Sham DFT is based on the assumption that the exact ground state electron

density can be represented by a ground state electron density of an auxiliary system of non-interacting particles moving in a mean effective potential $\hat{V}_{eff}$, which includes the problematic many-body exchange and correlation terms (see Fig. 2.3). The corresponding density calculated from the single-particle wave functions can be expressed as:

$$\rho(r) = \sum_{i}^{n} \left| \Psi_i^{KS}(r) \right|^2 \tag{2.12}$$

The density of the non-interacting system defines the effective potential, and in turn, the effective potential also defines the single-particle orbitals $\Psi_i^{KS}(r)$ through solution of the non-interacting Hamiltonian. The ground state density of the auxiliary system is equal to the exact many-body ground-state density, so solving the non-interacting system determines all properties of the many-body system.

The main advantage of Kohn-Sham DFT is to subdivide the full electronic problem into *n* coupled equations which each only depend on the coordinates of one orbital. The non-interacting part of the electronic kinetic energy thus becomes:

$$T_S = -\frac{1}{2}\sum_{i}^{n} \left\langle \Psi_i^{KS} \middle| \nabla^2 \middle| \Psi_i^{KS} \right\rangle = \frac{1}{2}\sum_{i}^{n} \int d^3r \left| \nabla \Psi_i^{KS}(r) \right|^2 \tag{2.13}$$

The second term in many-body description $\hat{V}_{ee}$ could be replaced by the classical interaction of the electron density $\rho(r)$ as:

$$E_{Hartree} = \frac{1}{2}\int d^3r d^3r' \frac{\rho(r)\rho(r')}{|r - r'|} \tag{2.14}$$

Combined with the exchange-correlation energy E_{xc}, the full Kohn-Sham energy functional could be written as:

$$E_{KS} = T_S[\rho] + E_{Hartree}[\rho] + \int d^3r \hat{V}_{eN}(r)\rho(r) + E_{xc}[\rho] \tag{2.15}$$

With this we arrive at the corresponding Schrödinger-like Kohn-Sham equation:

$$\left(-\frac{1}{2}\nabla^2+\hat{V}_{eff}(r)\right)\left|\Psi_i^{KS}(r)\right\rangle=$$
$$\left(-\frac{1}{2}\nabla^2+\hat{V}_{Hartree}(r)+\hat{V}_{eN}(r)+\hat{V}_{xc}(r)\right)\left|\Psi_i^{KS}(r)\right\rangle=\varepsilon_i\left|\Psi_i^{KS}(r)\right\rangle \quad (2.16)$$

In the Kohn-Sham approach to many-body systems, the remaining contribution to the energy, that is the difference between the exact and non-interacting kinetic energy and the non-classical part of the electron-electron interaction, are grouped together in a quantity known as the exchange-correlation energy functional.

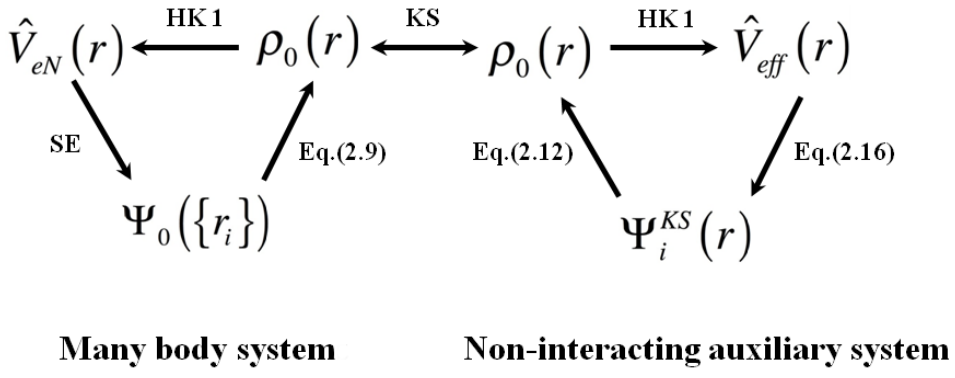

Figure 2.3 Illustration of the Kohn-Sham approach. Through the assumption that the ground state density of both the many body system and the non-interacting auxiliary system are equal, the two systems are connected through the Kohn-Sham ansatz. In this way, all properties of the many-body system can be determined by solving the non-interacting system.

2.2.4 Approximations to the exchange-correlation functional

The major challenge with Kohn-Sham DFT is to derive approximations to the exchange-correlation functionals. Various functionals with different complexity have been developed, and these can be sorted according to the Jacob's ladder scheme (see Fig 2.4) proposed by Perdew et al.[60-61]

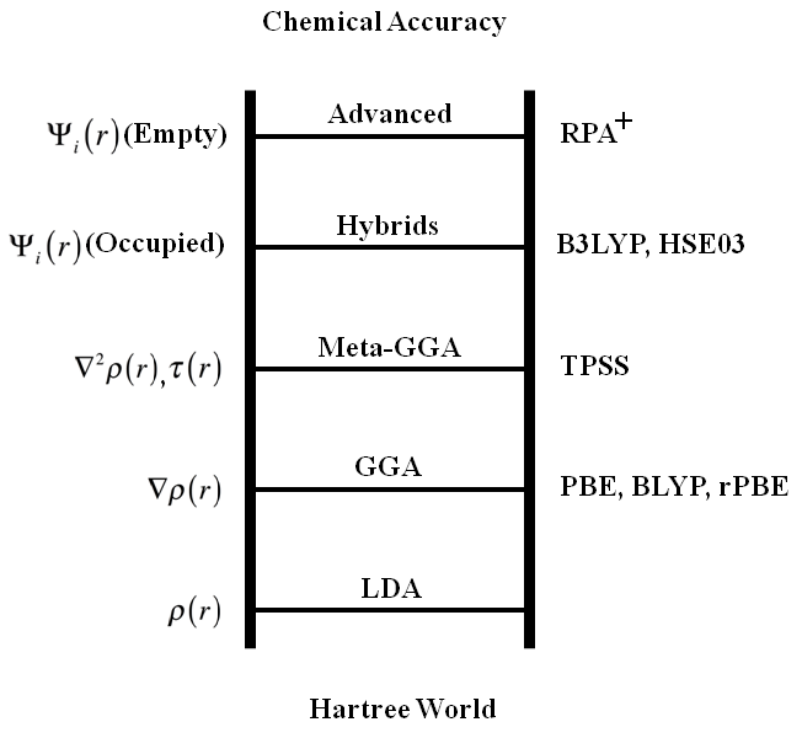

Figure 2.4 Jacob's ladder of DFT approximations to the exchange-correlation functionals.

The lowest rung in the Jacob's ladder is the so-called Local Density Approach (LDA), in which the functional only depends on the density at the coordinate where the functional is evaluated:

$$E_{XC}^{LDA}[\rho] = \int \varepsilon_{XC}^{LDA}[\rho(r)]\rho(r)d^3r \tag{2.17}$$

Although the LDA is based on a precarious assumption, it still predicts crystal structures quite well, deviating only a few percent from the experimental values[62].

On the second rung in the Jacob's ladder, Generalized Gradient Approximation (GGA) functionals are found. This class of functionals further incorporate information about the gradient of the density.

$$E_{XC}^{GGA}[\rho] = \int \varepsilon_{XC}^{GGA}[\rho(r),\nabla\rho(r)]\rho(r)d^3r \tag{2.18}$$

There are several forms of $\varepsilon_{XC}^{GGA}[\rho(r),\nabla\rho(r)]$ using one or more free parameters to include the gradient, but some of the most commonly used ones are PBE,[63] BLYP,[64-65] and rPBE.[66] Comparing with LDA, GGAs especially perform better for binding energies, where a too strong binding is often found with LDA.

On the next rung meta-GGA functionals are found, in which the second derivatives or the Kohn-Sham orbital kinetic energy density $\tau(r)=\frac{1}{2}\sum_i\left|\nabla\Psi_i^{KS}\right|^2$ is included.

$$E_{XC}^{meta-GGA}[\rho]=\int\varepsilon_{XC}^{meta-GGA}\left[\rho(r),\nabla\rho(r),\nabla^2\rho(r),\tau(r)\right]\rho(r)d^3r \tag{2.19}$$

Examples of functionals found on this rung are TPSS and the Minnesota functionals.[67]

Functionals on the fourth rung further include the exact electron exchange of occupied orbitals calculated from Hartree–Fock theory, Functionals of this type are known as hybrid functionals, i.e., B3LYP,[68] HSE03. These functionals present a huge improvement in many cases, including binding energies in molecules, the prediction of band gaps of semiconductors, etc. Yet, these functionals cannot describe metals quite well because Hartree–Fock always introduces an energy gap between the highest occupied and lowest unoccupied Kohn-Sham state (band-gap). Finally, functionals on the fifth rung of Jacob's ladder use the information from non-occupied orbitals as well. With the increase of the rung, the computational effort to solve the corresponding Kohn-Sham equation also increases significantly. Typically, one needs to make a comprise between the computational costs and the accuracy needed for the system of interest.

2.3 Calculating the electronic ground-state

2.3.1 Iterative approach to solving the Kohn-Sham equations

To calculate the ground state electron density and total energy of the studied system, the set of Kohn-Sham equations Eq. (2.16) needs to be solved iteratively. This is because each equation itself contains the density that it aims to calculate. Instead of simply calculating the eigenstates and eigenvalues of the operator, the equation needs to be solved iteratively to find the self-consistent potential resulting in the self-consistent density. Starting from a suitable guess for the density ρ_{in}, through diagonalization of the Kohn-Sham equation, one obtains a new density ρ_{out}, which will be used as the new initial density ρ_{in-new}. Using ρ_{in-new}, a new Kohn-Sham operator is constructed and the corresponding KS equation needs to be solved. The procedure repeats itself until the predefined convergence criteria is reached, then the self-consistent field (SCF) cycle is considered to be converged (see Fig 2.5).

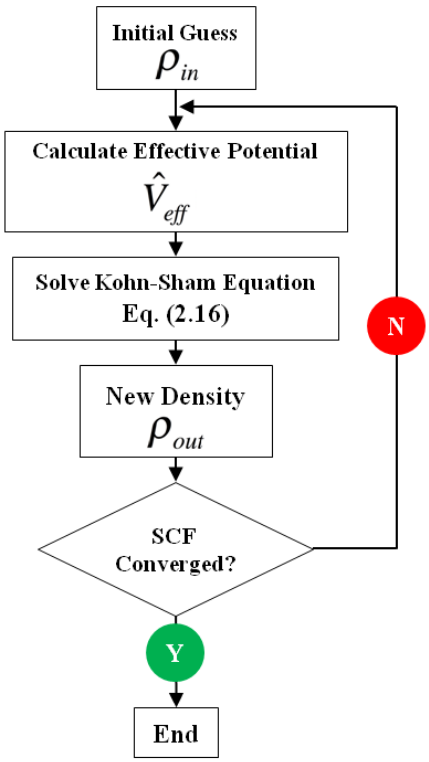

Figure 2.5 Self-consistent field cycle for solving the Kohn-Sham equations.

2.3.2 Basis sets and boundary conditions

In a numerical realization of DFT, self-consistently solving the set of linear differential equations in Eq.(2.16) has two prerequisites: boundary conditions and a certain representation of the Kohn-Sham states. In general, Kohn-Sham states can always be represented on a real-space grid, which then requires solving the differential equations on every grid point. Instead, the most commonly used method is to linearly expand the Kohn-Sham states Ψ_i into a sum of known basis functions φ_α:

$$\Psi_i(r) = \sum_\alpha c_{i\alpha}\varphi_\alpha(r) \tag{2.20}$$

The reason for expanding the wave function into a basis set is to turn the differential equation into an algebraic equation which is easier to solve on a computer. There are different options. In principle, any complete set of functions can be chosen as the basis sets to reproduce the differential equation to any desired precision. In principle the basis set expansion is thereby infinite, but for practical calculations it needs to be truncated. Therefore, the size of the basis set is a major parameter of convergence in a DFT calculation. To reduce the computational costs while maintaining the required accuracy,

convergence tests always have to be conducted.

DFT was first applied to solid-state crystals that have periodic structures. For such crystals, the Wigner-Seitz like unit cell and Born-von Karman periodic boundary conditions (PBC) need to be taken into consideration.[69-70] Felix Bloch[71] proposed that plane waves could be used as the basis functions, since they intrinsically match PBC and also describe the band-structure (delocalized in real-space):

$$\varphi_k(r) = \exp(ikr) \tag{2.21}$$

By doing this, translational symmetry is automatically exploited. Successfully solving the infinite crystal requires accurate sampling of the reciprocal space. The most commonly used scheme for generating **k**-points in the Brillouin zone has been proposed by Monkhorst and Pack,[72] which makes use of time reversal and inversion symmetry to reduce the number of grid points in **k**-space. To faithfully represent the full 3-dimensional band structure, the number of **k**-points needs to be tested carefully for every system by systematically increasing the grid-point density until the change of the corresponding quantities are within the range of the predefined criteria.

For a periodic surface, which can be considered as a truncated crystal lattice, we use a set of plane-waves as basis-vectors. There are several advantages: First of all, plane waves constitute an orthogonal basis, meaning that their overlap matrix is the identity matrix. Secondly, with plane waves in the form

$$\varphi_G^{(jk)} = \sum_G \frac{c_{G'}^{(jk)}}{\sqrt{\Omega}} \exp\left(i(G+k)\bullet r\right) \tag{2.22}$$

the corresponding Kohn-Sham equations can be transformed into Fourier space:

$$\sum_G \left[\frac{\hbar^2}{2m_e} |k+G|^2 \delta_{G,G'} + V_{KS}[\rho](G-G') \right] c_{G'}^{(jk)} = \varepsilon^{(jk)} c_G^{(jk)} \tag{2.23}$$

Then the kinetic energy of a plane wave becomes diagonal, so the computational cost for its evaluation is trivial. Thirdly, there exist highly optimized Fast Fourier Transform algorithms to transform between reciprocal and real-space.[73-74] Furthermore, plane waves are an extremely systematic basis set and **k** is the only parameter defining a plane wave, thus it is convenient to check convergence of any observable with respect

to the basis set size. In practical calculations, we need to control the precision of the plane wave basis. This can be done by using a cut-off energy E_{cut}, which fulfills the following conditions:

$$|G| < \sqrt{\frac{2m_e E_{cut}}{\hbar^2}} \tag{2.24}$$

However, with regards to an accurate and practicable description of the electronic structure in the presence of the bare Coulomb potential of the nucleus, plane waves do not work well. This is because the Fourier transform of a cusp in the electron density at the position of a nucleus cannot be truncated in **k**-space. In another words, an infinite number of plane waves are needed to describe the proper electron distribution. To ultimately remove the Coulomb singularity, plane waves are therefore normally used together with the pseudopotentials approximation, applying effective potentials of the nucleus plus core-electrons.

2.3.3 Pseudopotentials

As described above, the Coulomb potential of the bare nucleus and its respective singularity leads to issues when applying plane waves. For that Kleinman and Philips[75] proposed an approach to divide the electronic states into the valence electronic states and core electronic states. For most applications only the valence electrons participate in chemical reactions, while the core electron shells are 'frozen'. Thus it is not necessary to explicitly describe all electrons in the system, but only the valence electrons. The influence of the core electrons can be incorporated through a pseudopotential (effective core potential). The prerequisite for the pseudopotential is, of course, that the valence electrons in the presence of the pseudopotential behave just like in an all-electron description. Under this prerequisite, one way to construct the modified valence state $|\varphi_v'\rangle$ can be described as follows:

$$|\varphi_v'\rangle = |\varphi_v\rangle + \sum_c \langle\varphi_c|\varphi_v'\rangle|\varphi_c\rangle \tag{2.25}$$

Here $|\varphi_v\rangle$ is the valence electronic state and $|\varphi_c\rangle$ is the core electronic state.

With the modified valence state $|\varphi_v'\rangle$, the new potential can be expressed as:

$$V_{PS} = \sum_{c} (E_c - E) \langle \varphi_c | \varphi_v' \rangle | \varphi_c \rangle / | \varphi_v \rangle \tag{2.26}$$

and the modified Schrödinger equation for the valence states is:

$$\left(\hat{H} + V_{PS} \right) | \varphi_v \rangle = E | \varphi_v \rangle \tag{2.27}$$

Since only the valence states change according to the chemical environment, the core state can be calculated once and for all, and then be reused for all nuclear configurations.

Nowadays the most popular pseudopotentials are '*ab initio*' pseudopotentials, derived from an atomic reference state and requiring that the pseudo- and all-electron valence eigenstates have the same energies and densities outside a chosen core cut-off radius R_c. Hamann, Schlüter and Chiang[76] provided a corresponding list of mathematical requirements for an accurate *ab-initio* pseudopotential:

1. The pseudo- and all-electron valence eigenvalues agree for the chosen atomic reference configuration.

2. The pseudo- and all-electron valence wavefunctions agree outside a chosen core radius R_c.

3. The integrated charges within R_c agree for pseudo- and all-electron valence states.

4. The logarithmic derivatives of the pseudo- and all-electron valence states agree at R_c.

5. The first energy derivative of the logarithmic derivatives agree at R_c.

The larger the cut-off radius R_c is, the softer the pseudopotentials is, and the more rapidly it can be converged. But the disadvantage of softer pseudopotentials is that they are less transferable, meaning that they can less accurately reproduce realistic features in different environments.

The most common forms of pseudopotential used in modern plane-wave electronic structure codes like CASTEP are norm-conserving and ultrasoft pseudopotentials. Both of them allow proper numerical convergence with reasonable computing resources by using a basis-set with a significantly lower cut-off. Norm-conserving pseudopotentials

fulfill the condition that the norm of each pseudo-wavefunction is identical to its corresponding all-electron wavefunction inside the cut-off radius R_c.[77] Ultrasoft pseudopotentials further reduce the necessary basis-set size by relaxing this norm-conserving constraint.[78]

2.4 Transition state location

One of the biggest challenges in pursuing practical first-principles multi-scale simulations of heterogeneous catalysis is to obtain accurate transition states, since this can be cumbersome and computationally expensive. Here we will introduce the methods we are using in this thesis for locating the transition state.

2.4.1 Drag method

The most intuitive and simplest method for transition state search is what we will refer to as the Drag method. Within the framework of this method, one degree of freedom，i.e. the drag coordinate, is fixed, while all other degrees of freedom are relaxed. The drag coordinate is increased or decreased in small steps, while the system is being dragged from reactant to product or reverse. One of the most commonly used choices of the drag coordinate is simply to do a linear interpolation between the initial and final state. This is a less biased way and all Cartesian coordinates of the system then contribute to the drag coordinate. Another intuitive choice is to use a guess for a good reaction coordinate, for example, atoms that start out forming a bond which ends up being broken. The maximum energy obtained is then considered to be the saddle point energy. However, neither the intuitive assumed reaction coordinate nor the unbiased straight linear interpolation can promise a good reaction coordinates. Nevertheless, although there exists much more reliable methods, e.g. the Nudged Elastic Band Method discussed below, there are still some special cases where the Drag method is advantageous to use. In our work considering the energy barrier for Eley-Rideal type of reactions, the Drag method works better than NEB method because the latter has problems to converge as the regimes in terms of forces on the surface and in the gas phase are quite different.

2.4.2 Nudged Elastic Band (NEB) method

One of the predominant approaches for transition state search at present is the

Climbing Image Nudged Elastic Band (CI-NEB) method, which is an evolution from the original Nudged Elastic Band (NEB) method.[79] As compared to the NEB method, CI-NEB cures common failures resulting in sub-optimal convergence[80] and also makes it possible to find the exact transition state.[43] The key inputs for CI-NEB are initial and final states, and the main technical parameters that need to be chosen carefully according to the studied system are the spring constant and the number of images.

Normally before performing a CI-NEB, it is highly recommended to do some minimization with the regular NEB method to obtain a good estimate of the reaction coordinate around the saddle point. NEB is a chain-of-states method[81] which optimizes a chain of atomic configurations approximating the minimum energy path (MEP) between initial and final state.[79] Along the chain of the states, neighboring images are artificially coupled by a harmonic potential so as to keep these images roughly equidistant along the MEP. There are two types of forces that NEB takes into consideration: true atomic forces and spring forces. They are projected in two ways to solve the following two problems: on one hand, the elastic band tends to cut corners and gets pulled off the MEP by the spring forces in regions where the MEP is curved. On the other hand, the images tend to slide down towards the endpoints, giving lowest resolution in the region of the saddle point where it is most needed. The force on each image should only contain the parallel component of the spring force and the perpendicular component of the true force. This is because the component of the spring force perpendicular to the path induces the corner-cutting, and the parallel component of the true force coming from the interaction between atoms induces the down-sliding. The procedure for a NEB calculation can be described as follows: NEB first relaxes each image according to artificial forces, then new tangents are calculated and used to determine the artificial force. The above processes are repeated until the artificial forces are zero, so that the MEP is found.

The climbing image NEB (CI-NEB) method drives the image with the highest energy up to the maximum energy configuration by one modification. When turning on CI, the image with the highest energy does not see the spring forces along the band, while the true force at this image along the tangent is inverted. In this way, the image tries to maximize its energy along the band, and minimize it in all other directions, so this image will be at the exact saddle point when it converges.

3

Multi-scale modeling methods in mesoscopic regime

3.1 *Ab initio* thermodynamics

3.1.1 Surfaces at reaction conditions

From static DFT alone one can only obtain physical quantities of the studied nuclei at *T = 0 K* and *p = 0 atm*. To actually describe situations of finite gas-phase temperatures and pressures, DFT data can be integrated into thermodynamic considerations. Using this so-called '*ab initio* thermodynamics' approach, one can obtain the equilibrium geometry and composition of a solid surface in contact with a given environment at finite temperature and pressure, and thus determine the steady-state phase diagram of the surface under reaction conditions.

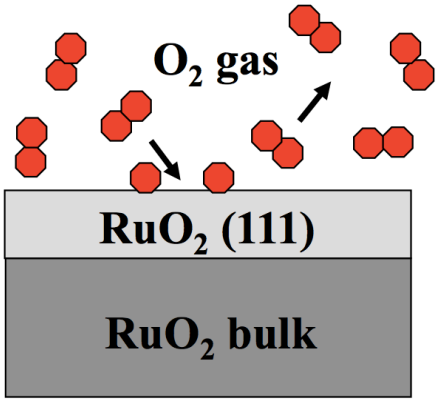

Figure 3.1 Schematic representation of the example system. O_2 can dissociatively adsorb on RuO_2(111), correspondingly, O atoms on RuO_2(111) might also associatively desorption. As a result, RuO_2(111) can present O-rich, stoichiometric or O-poor terminations at various $\left(T, p_{O_2}\right)$ conditions.

Here we use RuO_2(111) surface in contact with a surrounding O_2 gas phase as an example to illustrate the idea behind *ab initio* thermodynamics (see Fig. 3.1). Under given $\left(T, p_{O_2}\right)$ conditions, the Gibbs free energy of the entire system can be broken down into the contributions from the RuO_2 bulk G_{RuO_2-bulk}, from the RuO_2 (111) surface $G_{RuO_2(111)}$, and from the gas phase G_{O_2}.

$$G = G_{RuO_2-bulk} + G_{RuO_2(111)} + G_{O_2} \tag{3.1}$$

Then the surface free energy per unit area can be expressed as:

$$\gamma = \frac{1}{A}(G - G_{RuO_2-bulk} - G_{O_2}) \tag{3.2}$$

Here A is the area of the surface unit cell. Due to the distance from the surface, both the bulk solid and the gas phase part will not be affected by the created surface, so these contributions effectively cancel out in Eq. (3.2). Then Eq. (3.2) can be rewritten in terms of near-surface components as:

$$\gamma(T, p_{O_2}) = \frac{1}{A}\left[G_{RuO_2(111)}(T, p_{O_2}, N_{Ru}, N_O) - N_{Ru} G_{RuO_2-bulk} + (2N_{Ru} - N_O)\mu_O \right] \tag{3.3}$$

Here μ_O is the O chemical potentials; and N_{Ru} and N_O are the number of Ru and O atoms in the solid near the surface.

3.1.2 Calculating Gibbs free energies

To obtain the surface free energy in Eq. (3.3), the chemical potential of the oxygen environment as well as the Gibbs free energy of the solid bulk and surface need to be calculated.

3.1.2.1 Gas phase chemical potential

The chemical potential of oxygen at given temperature *T* and pressure *p* can be written as:

$$\mu_O(T, p) = \frac{1}{2}\mu_{O_2(gas)}(T, p) = \frac{1}{2}\left\{ \frac{1}{N}\left[k_B T \ln\left(\frac{1}{N!}\left(q^{trans}\right)^N \right) - pV \right] + \mu^{rot} + \mu^{vib} + \mu^{electr} + \mu^{nucl} \right\} \tag{3.4}$$

including the translational partition function q^{trans}, rotational free energy μ^{rot}, vibrational free energy μ^{vib}, electronic free energy μ^{electr} and nuclear free energy μ^{nucl}. The translational partition function q^{trans} in the thermodynamic limit equals to:

$$q^{trans} = V\left(\frac{2\pi m k_B T}{h^2} \right)^{\frac{3}{2}} \tag{3.5}$$

The rotational term for linear molecules approximates to

$$\mu^{rot} \approx -k_B T \ln\left(\frac{k_B T}{\sigma^{sym} B_0}\right)$$

(3.6)

where σ^{sym} is a classical symmetry number, indicating the number of indistinguishable orientations that the molecule can have (for hetero-nuclear diatomic molecules, σ^{sym} =1, while for homo-nuclear diatomic molecules, σ^{sym}=2). B_0 is the eigenvalue that needs to be considered when diagonalizing the inertial tensor for linear molecules.

The vibrational contribution equals to

$$\mu^{vib} = E^{ZPE} + \Delta\mu^{vib} = \sum_{i=1}^{M}\left[\frac{\hbar\omega_i}{2} + k_B T \ln\left(1 - \exp\left(\frac{\hbar\omega_i}{k_B T}\right)\right)\right]$$

(3.7)

The first term arises from the zero-point vibrations, and *M* is the number of fundamental modes ω_i that form the harmonic oscillators.

The electronic free energy contains two parts, one from the ground state, while the other arises from a spin degeneracy of this ground state:

$$\mu^{electr} \approx E_{O_2}^{total} - k_B T \ln\left(I^{spin}\right) \tag{3.8}$$

Here I^{spin} is the term depending on the electronic spin degeneracy of the ground state. The nuclear term does not change in the here considered chemical situations. It is a constant factor that cancels out in Eq. (3.3).

If we bring the above terms all together to Eq.(3.4), we can obtain the chemical potential for oxygen formed with the total energy and zero-point vibrational modes of the gas phase molecule, as well as $\Delta\mu_O(T,p)$ which depends on temperature and pressure, available in thermochemical tables.[82]

$$\mu_O(T,p) = \frac{1}{2}E_{O_2}^{total} + \frac{1}{2}E_{O_2}^{ZPE} + \Delta\mu_O(T,p) \tag{3.9}$$

3.1.2.2 Gibbs free energies for solid bulk and surface

The solid phase Gibbs free energies are composed of the following contributing terms:[14, 83]

$$G = E^{total} + F^{vib} + F^{conf} + pV \tag{3.10}$$

Here E^{total} is the total energy, F^{vib} is the vibrational free energy, and F^{conf} is the configurational free energy. The dominant term in Eq. (3.10) is the total energy, which can be provided through the DFT calculations. In the difference Eq. (3.3) the other terms largely cancel[84] and are thus neglected in our following estimation of the surface free energy.

3.1.3 Surface free energy plots

Using the evaluated Gibbs free energies, we can obtain the structure and composition of our model system in contact with a given environment at finite temperature and pressure. The corresponding surface free energy, or more precisely Gibbs free energy of adsorption, can be expressed as:

$$\gamma(\Delta\mu_O) = \frac{1}{A}\left[E^{total}_{RuO_2(111)} - N_{Ru}E^{total}_{RuO_2-bulk} + \left(2N_{Ru} - N_O\right)\left(\frac{1}{2}E^{total}_{O_2} + \Delta\mu_O\right)\right] \tag{3.11}$$

Here $\Delta\mu_O$ is the oxygen chemical potential which can be calculated through JANAF thermochemical tables, and E^{total} is the total energy of a given surface configuration as directly obtained from a DFT calculations. Eq. (3.11) then allows to directly plot the Gibbs free energy of adsorption as a function of the oxygen chemical potential $\Delta\mu_O$.

Although theoretically the oxygen chemical potential $\Delta\mu_O$ can vary from minus to plus infinity, it only makes sense to consider it within certain boundaries. For a metal oxide, the suitable lower boundary of $\Delta\mu_O$ is defined by the decomposition of the oxide into the pure metal and gas phase oxygen, while the upper bound of $\Delta\mu_O$ is given by such gas phase conditions, in which the gaseous component is so highly concentrated that condensation is going to take place on the surface. This leads to the following constraints for our model system:

$$\frac{1}{2N_{Ru} - N_O}\left[G_{RuO_2(111)}(T, p_{O_2}) - N_{Ru}G_{RuO_2-bulk} + (2N_{Ru} - N_O)\left(\frac{1}{2}E^{total}_{O_2}\right)\right] \le \Delta\mu_O \le 0 \tag{3.12}$$

The surface free energy plot yields a straight line for each considered model, an example is shown in Fig. 4.1. At any given $\Delta\mu_O$, the lower the line, the more stable the model is.

3.2 First-principles kinetic Monte Carlo (1p-kMC) simulations

3.2.1 1p-kMC algorithm

1p-kMC simulations provide detailed micro-kinetic information (i.e., surface steady-state structure and composition, turnover frequency) by fully accounting for the correlations, fluctuations and explicit spatial distributions of the chemicals at the catalyst surface.[85] The central input for 1p-kMC are the individual rate constants of the elementary processes from first-principles calculations, including those for adsorption, desorption, diffusion and reaction. To limit for the number of inequivalent processes, 1p-kMC is often performed on a lattice model. Based on this model, the system undergoes a time evolution which is coarse-grained to the discrete rare-event dynamics. This evolution is governed by the Markovian master equation,

$$\frac{dP_i(t)}{dt} = -\sum_{j\neq i} k_{ij}P_i(t) + \sum_{j\neq i} k_{ji}P_j(t) \tag{3.13}$$

Here $P_i(t)$ is the probability-density function of the system at time *t* in state *i*, and k_{ij} is the rate constant from state *i* to state *j*. Starting from an initial configuration, a kMC simulation proceeds by picking up one of the possible elementary processes *p* with the rate constant r_p using a random number ρ_1 which fulfills the condition:

$$\sum_{p=1}^{k-1} r_p \leq \rho_1 \sum_{p=1}^{P} r_p \leq \sum_{p=1}^{k} r_p \tag{3.14}$$

Here $\sum_{p=1}^{P} r_p$ is the total rate summing over all *P* possible processes in the current configuration, and $\rho_1 \in [0, 1)$ is the first random number for picking up the stochastic process. The probability of choosing a process *k* is weighted by its rate r_k. The larger the rate is, the higher probability the process is selected. After this process is executed, the second random number $\rho_2 \in [0, 1)$ is chosen to update the clock:[86]

$$t \to t - \frac{\ln(\rho_2)}{\sum_{p=1}^{P} r_p} \tag{3.15}$$

Based on the generated new configuration, the corresponding total rate $\sum_{p=1}^{P} r_p$ needs to be determined. And then repeating the above steps of selecting a process and advancing the time, the system proceeds until a preset number of steps is reached (see Fig. 3.2).

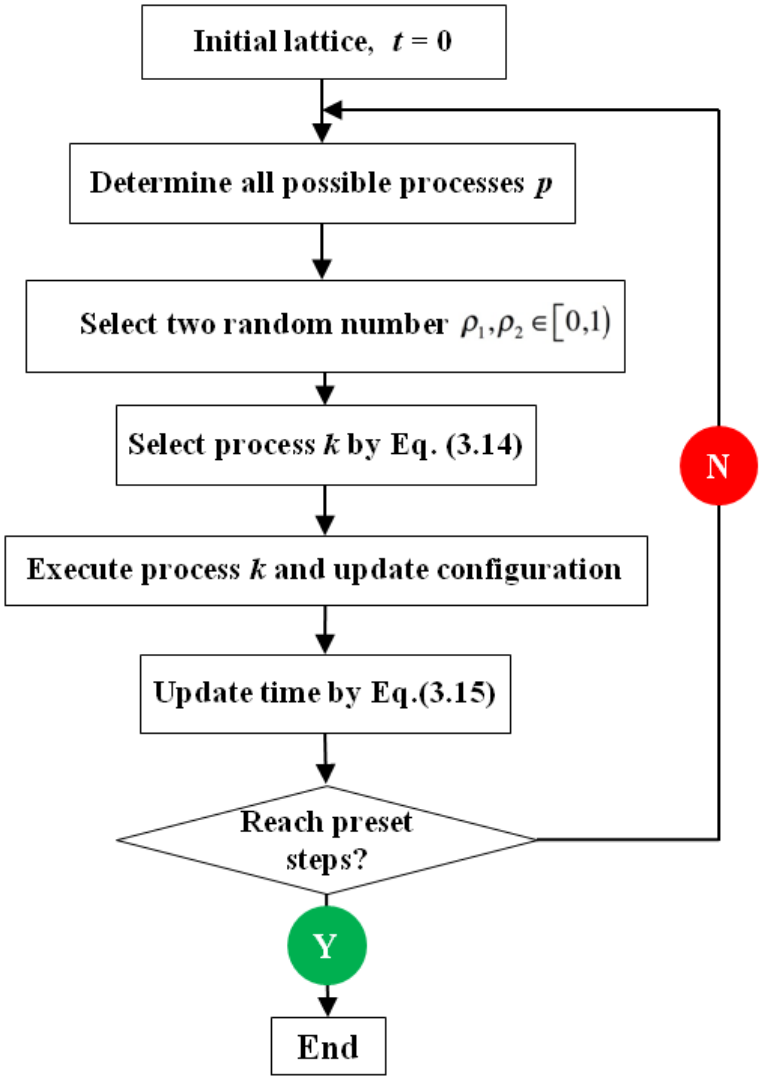

Figure 3.2 The basic steps of a kMC algorithm. From an initial configuration, the loop starts with the determination of all processes and their total rate constant. With two random numbers, the system configuration as well as the time is updated.

For a kMC simulation, the most crucial issue is to identify all possible relevant processes and their corresponding rate. To check the convergence of a steady-state kMC simulation, one needs to start from different configurations, and check if the kMC

simulation can eventually reach a unique steady state with constant surface coverages and turnover frequency.

3.2.2 First-principles rate constants

Understanding the essential idea behind 1p-kMC, we focus on the central input for it following the approach put forward by Reuter.[18, 35] Let's assume a surface is exposed to a composed gas of *i* different species with masses m_i. On top of this surface with a surface unit-cell area of A_{uc}, there are *st* different site types. At temperature *T* and partial pressure p_i, the adsorption rate of species *i* on a free site *st* can be expressed as:

$$r_{st,i}^{ads}(T,p_i) = \tilde{S}_{st,i}(T)\frac{p_i A_{uc}}{\sqrt{2\pi m_i k_B T}} \tag{3.16}$$

Here $\tilde{S}_{st,i}(T)$ is the local sticking coefficient, which governs the fraction of the impinging species that actually sticks to the given free site. For unactivated adsorption processes, the local sticking coefficient is approximated by the equipartitioned ratio of inequivalent sites in the surface unit cell; while for activated adsorption processes or Eley-Rideal type of reaction processes, it also depends on the adsorption or reaction barrier $\Delta E_{st,i}$:

$$\tilde{S}_{st,i}(T) = \left(\frac{A_{st,i}}{A_{uc}}\right)\exp\left(-\frac{\Delta E_{st,i}}{k_B T}\right) \tag{3.17}$$

Desorption of species *i* from a free site *st* is modeled as the time reversed process of the corresponding adsorption process, such that the desorption rate constant fulfills the microscopic reversibility:

$$\frac{k_{st,i}^{ads}(T,p_i)}{k_{st,i}^{des}(T,p_i)} = \exp\left(\frac{\Delta G_{st,i}(T,p_i)}{k_B T}\right) \approx \exp\left(\frac{\mu_i(T,p_i) - E_{st,i}^{bind}}{k_B T}\right) \tag{3.18}$$

Here $\Delta G_{st,i}(T,p_i)$ gives out the Gibbs free energy difference between the species *i* adsorbing on the surface and in the gas phase, approximated by the difference between the gas phase chemical potential $\mu_i(T,p_i)$[14] and the binding energy of species *i* at site *st* $E_{st,i}^{bind}$.

The diffusion rate constant for an adsorbed species *i* from site *st1* to site *st2* is approximated as:

$$k^{diff}_{st1\rightarrow st2,i}(T) \approx \left(\frac{k_B T}{h}\right)\exp\left(-\frac{\Delta E^{diff}_{st1\rightarrow st2,i}}{k_B T}\right) \quad (3.19)$$

Here $\Delta E^{diff}_{st1\rightarrow st2,i}$ is the corresponding diffusion energy barrier.

Similar to diffusion processes, the rate constant for Langmuir-Hinshelwood type of reactions of species *i* at site *st1* with species *j* at site *st2* is then approximated as:

$$k^{reac}_{i@st1+j@st2}(T) \approx \left(\frac{k_B T}{h}\right)\exp\left(-\frac{\Delta E^{reac}_{i@st1+j@st2}}{k_B T}\right) \quad (3.20)$$

with $\Delta E^{reac}_{i@st1+j@st2}$ being the reaction energy barrier.

Using the above approach to determine the rate constants for adsorption, desorption, diffusion and reaction processes, the required first-principles inputs are the binding energies of the species at the surface sites, as well as the energy barriers of activated adsorption, diffusion and reactions. The former one can be directly obtained through DFT calculations, while the latter one requires transition state searches as described above.

3.3 The kmos framework

In this thesis, we perform 1p-kMC simulations using the kmos[87] code developed by Max J. Hoffmann. The kmos code is an open-source package which has been developed for surface chemical reactions but could also be applied to other types of kMC models. The kmos code is a user-friendly implementation which allows to generate kMC models easily through a GUI. The runtime sensitively depends on the model complexity and thus needs to be systematically tested. For detailed information and the source code of kmos, please visit the following website: http://mhoffman.github.io/kmos/

II. RuO_2 particles at CO oxidation reaction conditions

In the following 2 chapters, we first reveal an intricate dependence of the RuO_2 crystal habit on the oxidizing pretreatment used in recent powder catalyst studies, and then concentrate our efforts on the catalytic mechanism of CO oxidation on one of the apical facets of RuO_2 particles, namely RuO_2(111).

In chapter 4, we present a DFT-based Wulff construction of the equilibrium shape of RuO_2 particles in an oxygen environment. The obtained intricate variations in the crystal habit with the oxygen chemical potential allow for a detailed discussion of the dependence on the oxidizing pretreatment used in recent powder catalyst studies. The analysis specifically indicates an incomplete particle shape equilibration in previously used low-temperature calcination. Equilibrated particles could be active CO oxidation catalysts with long-term stability in oxidizing feed and then represent an interesting alternative to the previously suggested core–shell concept.

In chapter 5, we present a density-functional theory based kinetic Monte Carlo study of CO oxidation at the (111) facet of RuO_2. We compare the detailed insight into elementary processes, steady-state surface coverages and catalytic activity to equivalent published simulation data for the frequently studied RuO_2(110) facet. Qualitative differences are identified in virtually every aspect ranging from binding energetics over lateral interactions to the interplay of elementary processes at the different active sites. Nevertheless, particularly at technologically relevant elevated temperatures, near-ambient pressures and near-stoichiometric feeds both facets exhibit almost identical catalytic activity. These findings challenge the traditional definition of structure sensitivity based on macroscopically observable turnover frequencies and allow to scrutinize the applicability of structure sensitivity classifications developed for metals to oxide catalysis.

4

Ab initio Wulff construction for RuO_2 nanoparticles under oxidizing conditions

4.1 Introduction

Systematic studies on polycrystalline powders are an appealing link between detailed surface science work on single crystals and the supported nanoparticles in real catalysis. They offer a general route to the exploration of important factors such as particle size, shape and composition without the additional complexity introduced by a support material. At present, such structure–morphology–activity relationships are only scarcely established. Not least, this is due to experimental difficulties in determining the crystal habit [i.e. particle shapes and (atomic scale) surface structure of the exposed facets] under reaction conditions. With ambient gas phases severely challenging the imaging and analytical capabilities of, for example, electron microscopes,[88] ex situ (either as prepared or post-mortem) studies still mostly provide the only access. This, however, neglects the attested possibly strong dynamical evolution of operating catalysts and the significant effect this can have on the catalytic function.[89-91] Even just the effect of catalyst pretreatments on surface phases and particle shapes is often not systematically explored, which determines the induction behavior during the dynamical evolution and which by itself may contain valuable information on the active sites involved.

In this situation, independent information from first-principles-based theory can be an enormous asset. To this end and complementing the experimental advances towards an in situ characterization, recent years have brought significant progress towards the consideration of finite gas phases in the corresponding electronic structure calculations.[92-93] DFT-based *ab initio* thermodynamic approaches[14, 44, 83] are now used readily to obtain the surface structure and composition of single-crystal model catalysts in contact with a multi-component gas phase environment. Combining the corresponding surface free energies within a Wulff construction then yields particle shapes in explicit dependence on temperature and reactant partial pressures.[32, 94-97]

Herein, we further explore this concept to address the largely different initial activities towards CO oxidation obtained in recent studies on polycrystalline RuO_2 powder catalysts by Narkhede et al.[25] and Rosenthal et al.[22, 98] They have been related to different calcination temperatures during catalyst preparation, which yields distinctly different crystal habits.[22, 25] Understanding these reactivity differences in terms of the

different facets and surface terminations exposed then offers an interesting new perspective on the controversially discussed active phases of Ru catalysts for this reaction. These catalysts demonstrate dramatic activity variations as a function of reactant pressure, which are generally assigned to a change in the oxidation state.[13, 99-100] However, despite significant efforts, consensus has not been reached regarding the detailed active state of the close-packed Ru(0001) facet,[1-3] that is whether it corresponds to the pristine metal with some coverage of oxygen adsorbates,[4] a more or less bulk-like film of RuO_2(110),[8, 22, 25, 101] or some intermediate (possibly badly defined) oxygen-enriched surface fringe involving sub-surface oxygen or a transient surface oxide.[6, 10, 17, 22, 98, 102] With RuO_2(110) itself clearly demonstrating high activity, this situation is further complicated by an enigmatic deactivation of supported Ru catalysts under oxidizing conditions,[7, 21] which was observed equally for polycrystalline RuO_2 particles.[9, 103]

For the RuO_2 particles, this deactivation has been assigned to a microfacetting of the lateral RuO_2(110) facets into inactive c(2x2)-RuO_2(100) phase.[9, 103] On the basis of our first-principles Wulff particle shapes, we argue that the presence of these lateral {110} facets (and the concomitant deactivation) could result from an incomplete particle shape equilibration at the used low calcination temperature. Different oxidizing pretreatments are found to affect the crystal habit critically by changing the cross section from quadratic to octagonal, as well as the share and type of facets exposed. Correlating this information with the reported activity data points towards an important role of the hitherto little studied {101} and {111} apical facets and specifically to their oxidation state under steady-state operation in net oxidizing or stoichiometric feed.

4.2 Computational details

With the approximations discussed in the preceding chapters, the working equation to evaluate the surface free energies entering the Wulff construction is as shown in Equation (4.1):[14, 44]

$$\gamma(\Delta\mu_O) = \frac{1}{2A}\left[E_{slab} - N_{Ru}E_{RuO_2(bulk)} + (2N_{Ru} - N_O)(\frac{1}{2}E_{O_2} + \Delta\mu_O) \right] \quad (4.1)$$

in which the factor 1/2 derives from the two sides of the symmetric slabs used to describe the surface system; A is the surface area; μ_O is the O chemical potential; and N_{Ru} and N_O are the number of Ru and O atoms in the solid with the surface. The required DFT input thus concerns the total energies of the surface system (E_{slab}), of RuO_2 bulk ($E_{RuO_2(bulk)}$) and of an isolated O_2 molecule (E_{O_2}). All these DFT calculations were performed by using the software package Cambridge *Ab Initio* Simulation Total Energy Program (CASTEP),[104] treating electronic exchange and correlation with the generalized gradient approximation functional due to Perdew, Burke and Ernzerhof.[63] The core electrons were described by using Vanderbilt ultrasoft pseudopotentials, whereas the valence electrons were treated with a plane-wave basis set with a cut-off energy of 450 eV. Supercell geometries with symmetric slabs and a vacuum separation exceeding 20 Å were used to describe the different surface orientations and (1x1) terminations. Specifically, we used five-layer slabs with (7x10x1), (10x5x1) and (6x7x1) Monkhorst–Pack reciprocal space sampling for RuO_2(100), RuO_2(110) and RuO_2(101), respectively, whereas seven-layer slabs with (7x7x1) and (6x6x1) Monkhorst–Pack reciprocal space sampling were used for RuO_2(001) and RuO_2(111), respectively. For each orientation, $E_{RuO_2(bulk)}$ was computed by using compatible k-meshes to allow for maximum error cancellation. By keeping only the middle slab layer fixed, all surfaces were fully relaxed until residual forces decreased below 0.05 eV $Å^{-1}$. E_{O_2} was computed spin-polarized in a (11x12x13) supercell with gamma-point sampling. Systematic tests showed the computed surface free energies to be converged within 5 meV$Å^{-2}$ at the used settings, which is sufficient for all conclusions made. The same holds with respect to the uncertainties owing to the used PBE functional. We also computed all surface free energies with the revised PBE functional[66] devised to cure the PBE over-binding of oxygen. Although the absolute surface free energies differed significantly, all conclusions with respect to the Wulff shapes remained untouched. The Wulff shape figures were created with WinXmorph.[105-106]

4.3 Results and discussion

The objectives of our study are the different RuO_2 particle shapes obtained after different calcination procedures as well as the different initial activities under net oxidizing feed conditions, under which the RuO_2 bulk structure was shown to be intact.

[22, 25, 98] Narkhede et al.[25] calcined in a 10 % O_2/Ne mixture at 573 K, whereas Rosenthal et al.[22, 98] used pure oxygen at 1073 K. We address these findings with a first-principles atomistic thermodynamic Wulff construction for RuO_2 particles in a pure oxygen environment.[32] Owing to the tetragonal symmetry of bulk rutile, this requires the determination of the surface free energies of the five inequivalent low-index surfaces: (100), (110), (111), (101) and (001). For each orientation, we consider all possible (1x1) terminations, which result from cutting the crystal stacking at different planes. For all five orientations, this yields an O-poor, a stoichiometric and an O-rich termination, whereas for the (111) orientation, a second even more O-rich termination (coined “super-O-rich”) is also possible. In this super-O-rich termination, the fivefold-coordinated (coordinatively unsaturated) surface Ru atom of the O-rich termination is capped by an on-top O atom at a bond length of 1.67 Å —a situation that occurs equivalently in the O-rich termination of the most studied RuO_2(110) surface.[14] Unfortunately, the geometric structure of the c(2x2)-RuO_2(100) reconstruction is as yet elusive, which is why we cannot compute its surface free energy explicitly. Instead, we derive bounds for its value on the basis of the obtained Wulff shapes below.

4.3.1 Surface free energies of RuO_2(111) terminations

In equilibrium with the surrounding O_2 gas phase, the most stable termination minimizes the surface free energy [Eq. (4.2)].[14, 44]

$$\gamma(T,p)=\frac{1}{A}\left[G(T,p,N_{Ru},N_O)-N_{Ru}\mu_{Ru}(T,p)-N_O\mu_O(T,p)\right] \tag{4.2}$$

Herein, A is the surface area; G is the Gibbs free energy of the solid with the surface; μ_{Ru} and μ_O are the Ru and O chemical potentials, respectively; and N_{Ru} and N_O are the number of Ru and O atoms in the solid with the surface. For not too low temperatures and sufficiently large particles, we can assume the surface to be equilibrated with bulk RuO_2, which enables the elimination of μ_{Ru} in Equation (4.2) in favor of the Gibbs free energy of bulk RuO_2.[32] By neglecting vibrational free energy contributions in the difference of bulk and surface Gibbs free energies, the remaining difference in total energies entering Equation (4.2) is computed within semi-local DFT [here the Perdew–Burke–Ernzerhof (PBE) functional; see the computational details Section]. [14, 44]

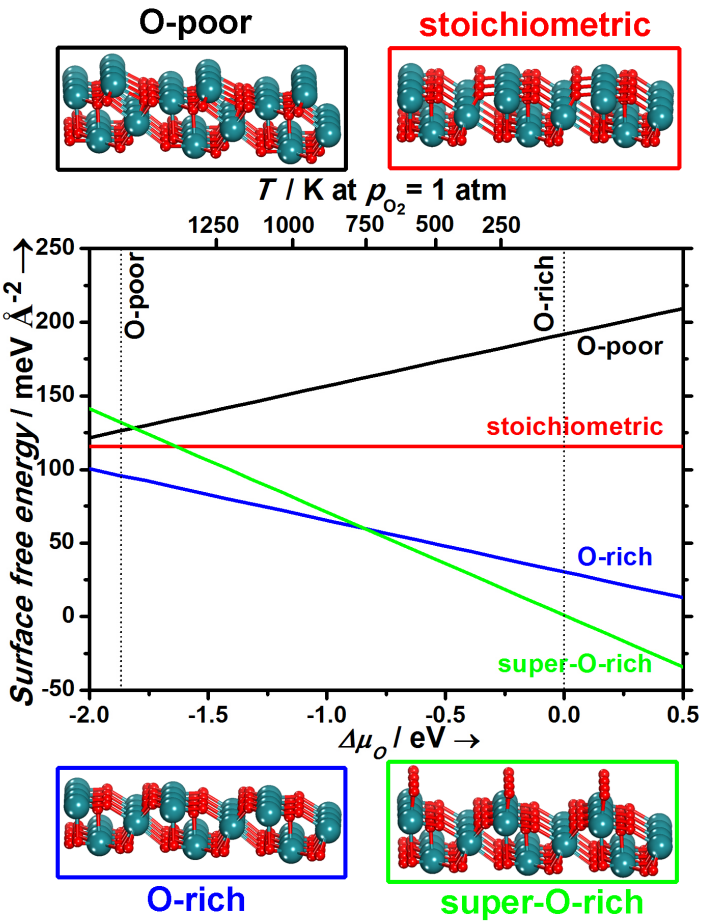

Figure 4.1 Surface free energies and surface geometries of the four possible (1x1) terminations of RuO_2(111). The dependence on the O chemical potential is converted into a temperature scale at P_{O_2} = 1 atm in the upper x-axis. The vertical dotted lines represent the $\Delta\mu_O$ range considered in our study, with the O-poor limit denoting the stability limit of bulk RuO_2 (see text).

The effect of the surrounding gas phase enters through the free energy contribution $\Delta\mu_{O_2}(T,p)$ to the oxygen chemical potential $\mu_O(T,p) = \frac{1}{2}E_{O_2} + \frac{1}{2}\Delta\mu_{O_2}(T,p)$, in which E_{O_2} is the total energy of an isolated O_2 molecule (including zero-point energy). The resulting dependence on the oxygen chemical potential for the surface free energies of the four terminations considered for the RuO_2(111) surface is illustrated Figure 4.1, in which ideal gas laws are used to directly convert this dependence into a temperature scale at fixed O_2 pressure of 1 atm (101.3 kPa). In addition, approximate but well-defined limits for the chemical potential range of interest are shown[14, 32]: The upper O-rich boundary roughly denotes the onset of oxygen condensation on the sample, and the lower O-poor boundary denotes the stability limit of bulk RuO_2 against decomposition into Ru metal, O_2 or volatile RuO_x species. All terminations except for the

stoichiometric termination demonstrate an explicit dependence on the O chemical potential, with, for example, the O-deficient O-poor termination becoming more favorable at higher temperatures. Through this dependence we obtain a change in the most favorable termination over the range of chemical potentials: At lower chemical potentials (higher temperatures) the O-rich termination results as most stable, whereas at higher chemical potentials (lower temperatures) this is the super-O-rich termination.

4.3.2 Wulff Construction for RuO_2 nanoparticles

The equivalent results obtained for all five low-index orientations are compiled in Figure 4.2. For each orientation we now directly show the minimized surface free energy; a change in slope reflects a change in the most stable termination. We obtain such a change in the most stable termination for all five orientations. For RuO_2(111), this is, as discussed, a transition from an O-rich to a super-O-rich termination. In all other cases this is a transition from stoichiometric to O-rich towards higher chemical potentials. This generalizes the findings reported earlier for the RuO_2(110) surface, namely the prediction of O-enriched (nominally polar)[14] terminations at higher chemical potentials, for example, for near-ambient O_2 pressures and temperatures below approximately 600 K (see Figure 4.2). The existence of such terminations reveals the shortcomings in the identification of the 'most stable' crystal faces on the basis of the surface energy of the stoichiometric termination.[107-108] The (environment-independent) computed surface energies of these terminations reflect the generally expected ordering, with the RuO_2(110) surface demonstrating the lowest value. The Wulff shape we obtain for this situation (corresponding to extremely low oxygen chemical potentials) agrees fully with the one published by Lopez et al.[109] However, as we exemplify below, this does not necessarily mean that {110} facets have a large share of the crystal surface for gas phase conditions corresponding to higher chemical potentials at which other terminations could get stabilized.

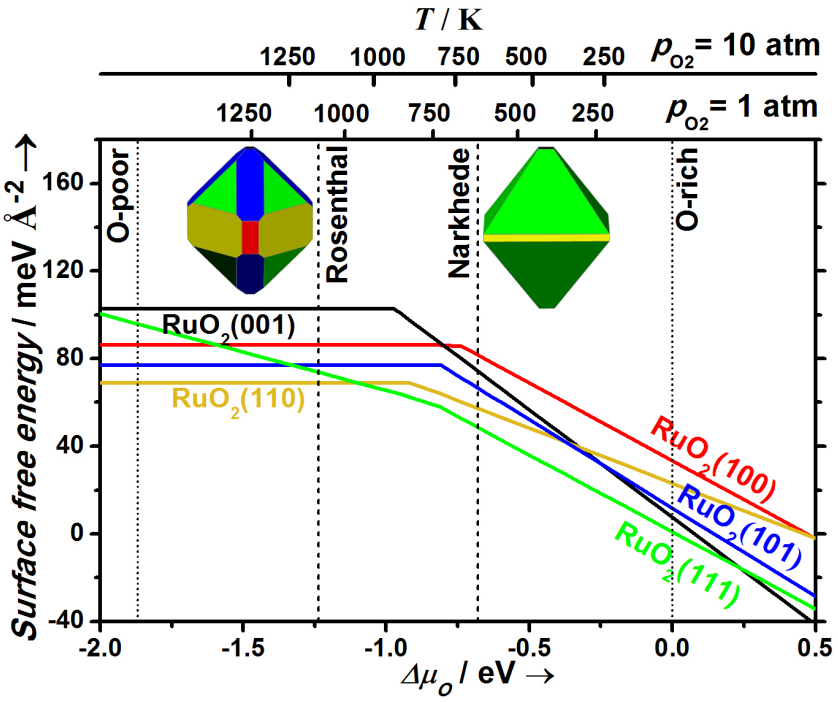

Figure 4.2 Same as Figure 4.1, but showing the minimized surface free energies for the five low-index RuO_2 surfaces. Also indicated by vertical dotted lines are the O chemical potentials corresponding to the calcination pretreatment used in the studies by Narkhede et al. and Rosenthal et al.: 0.1 atm, 573 K and 1 atm, 1073 K, respectively.[22, 25, 98] The insets show the corresponding particle shapes obtained from the constrained Wulff construction (see text), in which the colors of the different facets match those of the corresponding surface free energy lines.

With these results for different orientations, we proceed to evaluate a constrained Wulff shape that minimizes the total surface free energy for a given volume.[110] By 'constrained' we mean that the input to this construction is restricted to the surface free energies of the computed (1x1) terminations. Instead of determining the real equilibrium RuO_2 crystal shape, the purpose of the construction is therefore rather to compare the relative energies of the different (1x1)-terminated surface orientations and thereby establish a basis to discuss the effect of surface reconstructions on the crystal habit. Because the surface free energies depend on the oxygen chemical potential, the constrained Wulff shape can vary with the gas phase conditions and, in the present context, specifically with the applied calcination procedure.

As shown in Figure 4.2, notably different shapes are indeed obtained for the two procedures used in the powder catalyst studies. Apart from the similarity of a small {001} plateau capping the (symmetry-equivalent) apical sides, these differences extend

to both the exposed lateral and apical facets: Under the 0.1 atm, 573 K conditions used by Narkhede et al.,[25] the Wulff particle has a quadratic cross section and exhibits only {111} apical and {110} lateral facets. In contrast, under the 1 atm, 1073 K conditions used by Rosenthal et al.,[22, 98] the Wulff particle features {101} apical and {100} lateral facets, with the cross section concomitantly changed to irregular octagonal. The primary reason behind these rather significant differences in the crystal habit is the difference in terminations stabilized at the corresponding O chemical potentials. Under the conditions of the higher-temperature calcination, $\Delta\mu_O$ is low enough to stabilize the stoichiometric terminations at all low-index orientations apart from the {111} facets (see Figure 4.2). In contrast, the higher chemical potential corresponding to the conditions of the lower-temperature calcination already lies in the stability range of the O-rich terminations (or super-O-rich termination in the case of the {111} facets). The concomitant pronounced lowering of the (111) surface free energy preferentially stabilizes this apical facet, and the changed ratio of the surface free energies of the (110) and (100) orientations leads to the change in the cross section: For $1/\sqrt{2} < \gamma(100)/\gamma(110) < \sqrt{2}$, both facets are exhibited at irregular octagonal cross sections. For $\gamma(100)/\gamma(110) < 1/\sqrt{2}$ or $\gamma(100)/\gamma(110) > \sqrt{2}$, the cross section is quadratic, with only {100} or {110} facets exposed, respectively.

4.3.3 Comparison with experimental data

Overall, the obtained particle shapes are quite consistent with the electron microscopy images reported in the two powder catalyst studies.[22, 25] This holds for the cross sections and types of apical and lateral facets exposed. In both cases, however, the experimental shapes are much more columnar with a larger share of lateral facets. Habits similar to the ones of the Rosenthal crystals have been reported in earlier growth studies, which even involved higher calcination temperatures.[111-112] For the Rosenthal crystals, this renders kinetic limitations as an explanation for the difference to our computed Wulff shape unlikely. Instead, we attribute this difference to the previously reported restructuring of {110} facets into c(2x2)-{100} microfacets,[9, 103] which are not contained in our model. By neglecting the actual cost of the microfacetting itself, such a restructuring would equalize the (110) and (100) surface free energies at a lower value.

The concomitant change in the $\gamma(100)/\gamma(110)$ ratio towards 1 would make the cross section even more octagonal, and the surface free energy lowering of lateral facets would elongate the crystal shape. This is illustrated in Figure 4.3 b, in which the surface free energy of all lateral facets has been reduced at least to the value of the stoichiometric (110) termination. In reality, the surface free energy of the c(2x2)-(100) reconstruction must be (much) lower than this; otherwise there would be no thermodynamic driving force for the microfacetting of the {110} facets. As shown in Figure 4.3 c, there is, however, a lower bound for this value as well because a too-strong lowering of the surface free energy of the lateral facets would eliminate the {111} apical facets, which are clearly observed in the experiment. At $\Delta\mu_O$ = -1.24 eV corresponding to the Rosenthal calcination, this lower bound is obtained by lowering the surface free energy of the {100} facets for the stoichiometric (1x1) termination by 69 % from 86 to 27 meVÅ^{-2}.

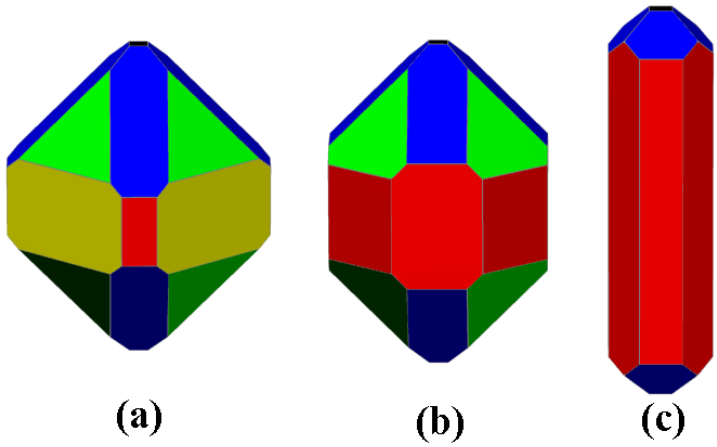

Figure 4.3 RuO_2 crystal shape at $\Delta\mu_O$ = -1.24 eV corresponding to the calcination pretreatment (1 atm, 1073 K) used in the Rosenthal experiments[22, 98]: a) First-principles constrained Wulff shape (see Figure 2). b) Shape resulting by reducing the surface free energy of all lateral facets to the computed value for γ(1x1)-(110) as minimum reduction induced by a restructuring and microfacetting to c(2x2)-(100) (indicated by drawing all lateral facets in the color code of the (100) facet ; see Figure 2). c) Shape resulting by further reducing the surface free energy of all lateral facets to the point at which the (111) apical facets disappear (see text).

In the Narkhede experiments, the reported more columnar, needle-like shape at quadratic cross section[25] is more difficult to reconcile within a thermodynamic picture with the almost cubic Wulff shape shown in Figure 4.2. In this case, the elongation

cannot be rationalized with the c(2x2)-(100) reconstruction. If this reconstruction was stabilized through microfacetting of the exposed {110} lateral facets, this should also hold for the {100} facets themselves, which invariably drives the particle cross section to octagonal. Until now, no other surface reconstruction of RuO_2 (110) has been reported under oxygen-rich conditions, thus it is difficult to ascribe the deviation from the constrained Wulff shape to a lowered surface free energy of lateral facets compared to the (1x1) terminations considered. Simultaneously, any missed reconstruction of apical facets would not help either, as this would only tend to further reduce the share of lateral facets. At the given quadratic cross section, this share is entirely determined by the $\gamma(100)/\gamma(110)$ ratio, which would need to be significantly lower to arrive at an elongated columnar shape. Considering the well-documented success of the used semi-local DFT functional in describing oxidation reactions at RuO_2 surfaces,[13, 99-100] we find it hard to assign such a large error, in particular in relative surface free energies, to its shortcomings. Instead, in our view a more likely explanation for the shape difference than unconsidered surface reconstructions modifying the Wulff shape within a thermodynamic picture is that the Narkhede crystals had not achieved their true equilibrium shapes but are dominated by kinetic limitations of the growth process. Also supported by possibly interesting catalytic function as discussed in the following, this motivates further experiments revisiting the shape–pretreatment relationship at low calcination temperatures. One possibility to overcome kinetic limitations at such temperatures could be to apply overpressures, which would enable similarly high oxygen chemical potentials but at higher temperatures. This is illustrated in Figure 4.2, in which an additional temperature scale for an O_2 pressure of 10 atm is shown.

The obtained constrained Wulff particle shapes and the discussed understanding of deviations in terms of surface reconstructions and kinetic limitations finally allow for a discussion of the catalytic activities reported in the powder catalyst studies.[22, 25, 98] Considering the established inactivity of the reconstructed c(2x2)-RuO_2(100) surface towards CO oxidation,[9, 103] the initial inactivity of the as-prepared Rosenthal crystals in oxidizing feed supports the view of a corresponding restructuring of all lateral facets during the redox pretreatment. In contrast, the immediate activity of the Narkhede crystals in such a feed is well rationalized by the initial presence of the highly active O-rich (1x1)-(110) termination at the lateral facets. As discussed by Aßmann et al.,[9, 103] the slow degradation in both stoichiometric and oxidizing feed would then be consistent with

the gradual reconstruction of the {110} facets to c(2x2)-(100) microfacets, which is accompanied by a morphology change to the octagonal habit.

With the lateral facets deactivated in either case, Rosenthal et al. ascribed the observed long-term catalytic function under oxidizing conditions to the apical facets.[98] The long induction time in such feed then suggests that the exposed, as-prepared {101} and {111} stoichiometric terminations are essentially inactive and only slowly transform to a more active phase. One possible candidate could be the c(1x2)-RuO_2(101) reconstruction, which Kim et al. found to be highly reactive.[101] However, this structure was achieved through high-temperature annealing in ultra-high vacuum and should thus rather correspond to an O-deficient composition. Intermediate temperature CO oxidation in net oxidizing feeds points towards the stabilization of O-enriched structures compared to those of the high-temperature calcination pretreatment. In this regard, it is intriguing to note that the super-O-rich RuO_2(111) termination (see Figure 4.1) features exactly the kind of singly coordinated (coordinatively unsaturated) O atoms that have served as the central rationalization for the known high activity of the RuO_2(110) surface.[13, 99-100] If this termination was active, the long induction times of the Rosenthal experiments could possibly be assigned to the stabilization of such O-enriched structures together with an increasing share of {111} facets at particles evolving towards their equilibrium shape at higher chemical potentials (see Figure 4.2).

Such a view puts even more emphasis on the discrepancy between the obtained constrained Wulff shape and the crystal habit reported by Narkhede et al.: If the columnar Narkhede crystals with their large share of lateral facets were an artefact of an incomplete crystal shape equilibration at the low calcination temperature, so would be the reported deactivation through the formation of the inactive c(2x2)-(100) phase at these lateral facets. The equilibrium shape obtained within the constrained Wulff construction under 0.1 atm, 573 K conditions barely features lateral facets. Actually, at only slightly lowered calcination temperatures (or slightly increased oxygen pressures), these facets become completely suppressed and the Wulff particles (apart from the small {001} apical cap) feature exclusively {111} apical facets. As such, it would be interesting to revisit the crystal morphology after high chemical potential calcination and the concomitant catalytic activity in oxidizing feed. If the first-principles constrained Wulff shape was validated and the O-enriched {111} facets were active as suggested by

Rosenthal et al.,[98] such pretreatment would result in catalyst particles that would not suffer from deactivation through the formation of the c(2x2)-(100) phase. In addition to the core–shell concept brought forward by Aßmann et al.,[9, 103] this could thus establish a second type of active RuO_2 catalyst with long-term stability in oxidizing feed.

4.4 Conclusions

We have used an *ab initio* thermodynamic Wulff construction to obtain the equilibrium shape of RuO_2 particles in an oxygen environment. The results indicate a sensitive dependence of the crystal habit on the O chemical potential, with different facets exposed and a change in the cross section from quadratic to irregular octagonal. Overall, these findings are fully consistent with the different crystal shapes reported for different calcination pretreatments in recent powder catalyst studies.[22, 25, 98] In detail, however, the experimental particles are much more columnar than the first-principles Wulff shapes. For the higher-temperature calcination used by Rosenthal et al.,[22, 98] this is likely rationalized by a microfacetting of lateral facets not contained in the present model. For the lower-temperature calcination used by Narkhede et al.,[25] this rather points towards an incomplete shape equilibration in the pretreatment.

Correlating the reported initial activities towards CO oxidation in oxidizing feed with this detailed insight about the crystal habit supports the interpretation of Rosenthal et al. in terms of a prominent role of the hitherto little studied {101} and {111} apical facets. We argue that the deactivation reported by Narkhede et al. could be an artefact of the incomplete particle shape equilibration reached in the pretreatment. This strongly suggests revisiting the morphology–activity relationship for high chemical potential calcination. If the first-principles Wulff shape is validated, this could yield a new type of active RuO_2 catalyst with long-term stability in oxidizing feed.

5

First-principles kinetic Monte Carlo simulations for CO oxidation at $RuO_2(111)$

5.1 Introduction

Detailed kinetic studies comparing the catalytic activity of different single-crystal facets provide important insights on several accounts. They allow for a straightforward assessment of the structure sensitivity of the catalytic reaction[113-116], which constitutes an important first milestone when aiming to relate the detailed knowledge from model catalysts to the performance of real supported catalysts. They also contribute to a more systematic bridging of the materials gap when employed to analyze data obtained for polycrystalline powders. This holds in particular if microkinetic models established for different facets are suitably combined to address the catalytic activity as a function of size and shape of the active nanoparticles. Recent years have seen the advent of predictive-quality first-principles microkinetic models.[93] Due to the still notable computational costs in obtaining the underlying first-principles data, such work has hitherto largely focused on the study of individual single-crystal facets. As a first step towards a full first-principles microkinetic model of a nanoparticle we here present a detailed first-principles kinetic Monte Carlo (1p-kMC) study of CO oxidation at RuO_2(111).

Over the years CO oxidation at RuO_2 has developed into a most extensively studied system, originally motivated to rationalize the qualitative activity differences of Ru catalysts in ultra-high vacuum and ambient conditions.[13, 99-100] Almost all of the single-crystal work has thereby been focused on RuO_2(110), which forms upon oxidation of the close-packed Ru(0001) surface and which constitutes the lateral facets of RuO_2 crystals. As this surface was shown to microfacet into an inactive c(2x2)-RuO_2(100) phase under oxidizing conditions[9], recent experimental[98] and theoretical[117] work has pointed at a possibly prominent role of apical RuO_2(111) facets for the long-term catalytic activity in such feeds. In the present work we therefore focus on this facet and compare extensively to the established 1p-kMC model for CO oxidation at the hitherto primarily investigated RuO_2(110) facet[18, 45, 85, 118]. In order to allow a most meaningful comparison, we thereby employ exactly the same microkinetic modeling approach, namely 1p-kMC[63, 119], and the same density-functional theory (DFT) exchange-correlation functional, namely the generalized-gradient functional due to Perdew, Burke and Ernzerhof (PBE)[63].

Previous work on structure sensitivity at metal catalysts has emphasized the role of electronic effects due to a different degree of under-coordination of surface atoms, as well as the role of geometric effects due to different bonding configurations.[120-121] At the structurally more complex oxide surfaces we find that the spatial distribution of the active sites and concomitant diffusion limitations constitute a third important factor. We identify qualitative differences in all three respects in the CO oxidation at RuO_2(111) and RuO_2(110). As such one would clearly classify the reaction as structure sensitive. However, the catalytic activities of the two facets peak with very similar maximum turnover frequencies (TOFs) at different reactant partial pressure ratios. This highlights that care has to be taken when assessing a potential structure sensitivity merely on the basis of comparable catalytic activity in a restricted range of feed conditions: At least for RuO_2(111) and RuO_2(110) near-ambient feed conditions can be found where depending on the exact partial pressure ratio both facets exhibit either virtually identical or largely differing TOFs.

5.2 Methodology

We evaluate the kinetics of the reaction network using 1p-kMC simulations.[93, 119] For steady-state reaction conditions defined by temperature and reactant partial pressures, (T,p_{O2},p_{CO}), the central outcome of such simulations are the overall catalytic activity (measured as TOF in product molecules per area and time) and average coverages at the surface. In contrast to prevalent mean-field rate equation based microkinetic simulations, 1p-kMC thereby fully accounts for the correlations, fluctuations, and explicit spatial distributions of the reaction intermediates at the catalyst surface.[85] This allows to analyze in detail the occurrence and contribution of any elementary process or local surface configuration within the entire reaction network. The input required for 1p-kMC simulations are a list of all elementary processes in the reaction network and their respective rate constants. We evaluate the latter using DFT and transition state theory (TST).[18] Additionally required is a lattice model that specifies the geometric arrangement of the individual surface sites involved in the reaction network. In the following we first summarize this lattice model and the list of elementary reactions considered, and then describe the computational procedure to obtain the first-principles rate constants.

5.2.1 Lattice model and elementary processes

The lattice arrangement of rutile RuO_2 along the [111] direction can be seen as a stacking of (RuO_4)-Ru bilayers as illustrated in Fig. 5.1a. Each bilayer is laterally displaced from the one underneath until the sequence repeats itself after four bilayers. Each RuO_4 plane exhibits three non-equivalent O atoms, which together with the Ru plane leads to a total of four possible RuO_2(111)-(1x1) terminations.[117] We choose the most stable O-poor termination involving the RuO_4 plane as basis for the 1p-kMC lattice-model, as this then naturally accommodates all other O-terminations as a consequence of O adsorption processes. As shown in Fig. 5.1b the chosen O-poor termination exposes three under-coordinated Ru atoms per surface unit-cell: One threefold coordinated Ru atom (labeled as Ru_2) and two fivefold coordinated Ru atoms (labeled as Ru_1 and Ru_3, respectively). Systematically exploring O and CO adsorption at all high-symmetry sites, our DFT calculations identified three possible adsorption sites close to these Ru atoms: A bridge site between Ru_1 and Ru_2 (labeled as site Ru_1Ru_2), a site atop of Ru_2 (labeled as Ru_2) and a bridge site between Ru_2 and Ru_3 (labeled as site Ru_2Ru_3). These are exactly the sites that would be occupied by O atoms in the continuation of the bulk stacking sequence, i.e. we did not find any additional adsorption sites stabilized as a consequence of the lattice truncation at the surface.

Figure 5.1c depicts the lateral arrangement of these three adsorption sites. Their linear arrangement in form of a Ru_1Ru_2–Ru_2–Ru_2Ru_3 site chain enables two-site processes like dissociative O_2 adsorption, associative O_2 desorption, O and CO diffusion, as well as Langmuir-Hinshelwood (LH) type CO oxidation at and between directly neighboring site pairs, but not at or between the most distant Ru_1Ru_2 and Ru_2Ru_3 site pair. Even more intriguing is the large geometric distance of any of these three sites to any site in neighboring surface unit-cells. As shown in Fig. 5.1c the closest such distances are between a Ru_2Ru_3 site in one cell and a Ru_1Ru_2 in the nearest-neighboring surface unit cell (3.30 Å), and between a Ru_2 site and a Ru_1Ru_2 site in the nearest-neighboring surface unit cell (4.69 Å). We tested for two-site processes involving these site pairs, but always obtained prohibitively large barriers. Only diffusion processes between Ru_2 and Ru_1Ru_2 sites across unit cells led to reasonable barriers and are accordingly considered in the 1p-kMC model.

Essentially, this thus leads to a lattice model for CO oxidation at $RuO_2(111)$ that has more of a molecular character than that of an extended surface network. Within the ensemble of three sites Ru_1Ru_2–Ru_2–Ru_2Ru_3 within one surface unit-cell we consider non-concerted adsorption, desorption, diffusion and reaction processes, with two-site processes restricted to nearest-neighbor pairs within the three-site chain. Specifically, dissociative O_2 adsorption can occur on empty Ru_1Ru_2–Ru_2 or Ru_2–Ru_2Ru_3 pairs, molecular CO adsorption on any empty site, and O/CO diffusion to a nearest-neighboring empty site. Desorption processes are modeled as time-reversed counterparts of the adsorption processes. LH oxidation reactions are possible between O and CO occupying nearest-neighbor sites and lead to an immediately desorbing CO_2 product molecule. Eley-Rideal (ER) oxidation reactions in form of gas-phase CO scattering are possible with O adsorbed at any of the three sites and lead equally to an instantaneously desorbing CO_2. The only additional processes that can connect sites in adjacent surface unit-cells are diffusion processes between Ru_2 and Ru_1Ru_2 sites. At the feed conditions discussed below, these diffusion processes have only a quantitative effect though. Switching them off in the 1p-kMC simulations left all conclusions put forward below intact and led to TOF changes at peak activities of the order of five. In practice, the lattice model can therefore be seen as a finite three-site model.

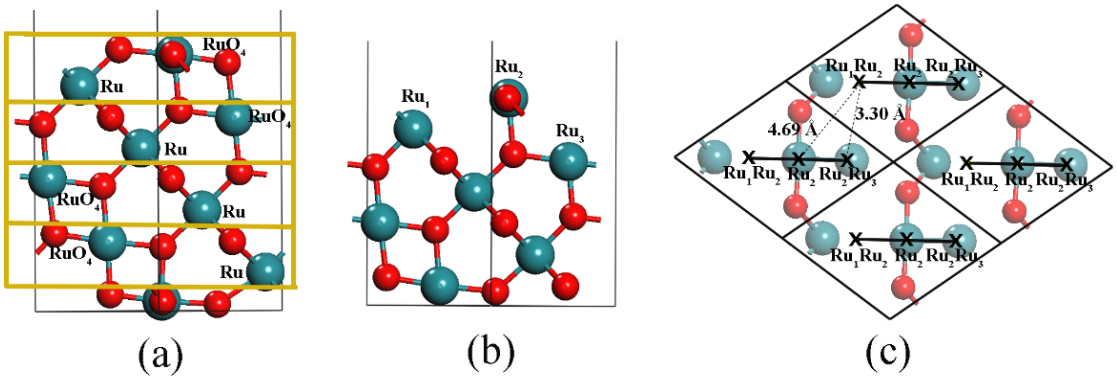

Figure 5.1 (a) Side view illustrating the stacking sequence of rutile RuO_2 (111) with every (RuO_4)-Ru bilayer marked with a yellow box to highlight the repeat sequence after four bilayers. (b) Side view of the most stable O-poor termination chosen as basis for the 1p-kMC lattice model (see text). (c) Top view showing four $RuO_2(111)$ surface unit-cells. Additionally marked are the three surface sites (Ru_1Ru_2, Ru_2, Ru_2Ru_3) considered in the 1p-kMC model and the shortest geometric distances across surface unit-cells. Ru atoms are shown as large blue spheres, O atoms as small red spheres.

5.2.2 First-principles rate constants and computational details

The calculation of the first-principles rate constants follows the approach put forward by Reuter and Scheffler[18]. This approach as detailed in chapter 3 relies on kinetic gas theory to determine the rate constants for adsorption processes and ER reaction processes. Rate constants for time-reversed desorption processes are determined through detailed balance. For bound-to-bound transitions like surface diffusion processes or activated LH reactions harmonic TST is applied. This reduces the first-principles input necessary to calculate the rate constants essentially to binding energies and reaction barriers. These energetic parameters are obtained from DFT using the plane-wave code CASTEP[104]. Electronic exchange and correlation is treated at the level of the PBE generalized gradient functional[63]. The core electrons are described by standard library ultrasoft pseudopotentials, while the valence electrons are expanded in a plane-wave basis set with a cut-off energy of 450 eV. The RuO_2(111) surface is modeled with a 7-bilayer slab with the bottom three layers fixed to represent the bulk structure, and a vacuum separation exceeding 10 Å. Reciprocal space integrations are carried out on a (4x4x1) Monkhorst–Pack grid for a (1x1) surface unit-cell. All adsorption geometries are fully relaxed until residual forces are below 50 meV/Å. With this computational setup the binding energies used to determine (thermodynamic) desorption barriers are converged to within 50 meV. We furthermore validated that this setup provides a binding energetics that is fully consistent with the full-potential approach that was employed for the RuO_2(110) 1p-kMC model[18]. Explicit surface barrier calculations for LH reaction and diffusion processes were carried out with the climbing-image nudged elastic band (CI-NEB) method[123] as implemented in the ASE environment[124] and using eight images between the known initial and final states. Activation barriers for ER reaction and adsorption processes were obtained through reaction coordinate scans of the potential energy surface. As reaction coordinates we employed constraints on the vertical distance from the surface or in case of ER also the C-O distance between the impinging CO and the adsorbed O atom.

Table 5.1 O_2 and CO desorption barriers (in eV). The different rows specify the sites out of which desorption occurs, while the different columns indicate the occupation of the other site(s) within the surface unit-cell (empty (e), O or CO). The variation over the different columns thus reflects the lateral interactions with nearby adsorbed species.

O_2 desorption barrier			
	e	O	CO
O_2@Ru_1Ru_2–Ru_2	2.96	3.30	2.94
O_2@Ru_2–Ru_2Ru_3	3.22	2.35	2.44

CO desorption barrier									
	e e	e O	e CO	O e	O O	O CO	CO e	CO O	CO CO
CO@Ru_1Ru_2	1.54	1.42	1.71	0.47	0.76	0.01	0.90	0.82	1.04
CO@Ru_2	1.88	1.90	1.59	1.01	1.32	0.85	1.24	1.30	0.92
CO@Ru_2Ru_3	0.98	0.99	0.69	1.49	0.96	1.33	1.15	0.53	0.83

No appreciable activation barriers were identified for the dissociative O_2 and molecular CO adsorption processes within the sites of one surface unit-cell. Within the hole model for adsorption underlying the Reuter/Scheffler approach[18], the sticking coefficients needed to determine the adsorption rate constants are then approximately given by the fraction of all impinging molecules that ends up in the corresponding sites/site pairs. For simplicity, we apply an equi-partition and use ½ for dissociative O_2 adsorption over the two site pairs Ru_1Ru_2–Ru_2 and Ru_2–Ru_2Ru_3, and ⅓ for the uni-molecular CO adsorption over each of the three sites within the unit-cell. Since adsorption is non-activated, all desorption barriers for the time-reversed processes are given by the thermodynamic binding energies. Due to the highly under-coordinated Ru_2 surface atom we calculate significant lateral interactions between the adsorbed species, i.e. the bond strength at the individual sites varies largely with the occupation of the other sites within the surface unit-cell. In contrast, there are only negligible lateral interactions between sites across surface unit-cells. Fortunately, the latter thus generates only a small number of different site occupations for which binding energies are required. For dissociative O_2 desorption these are three different binding energies of O_2 at the Ru_1Ru_2–Ru_2 pair, depending on whether the Ru_2Ru_3 site is empty, or occupied by O or CO. For dissociative O_2 desorption out of the Ru_2–Ru_2Ru_3 pair this is likewise three binding energies, while for the CO desorption out of the three sites a total of 27 binding energies are required (depending on the occupation of the other two sites). This small number of combinatorial possibilities can still be captured by explicitly calculating the binding energy of every configuration. This allows to exactly treat the large lateral interactions implied by the corresponding numbers compiled in Table 5.1, as compared to the more common approximate treatment in form of short-ranged lattice-gas Hamiltonians.[125-128]

Table 5.2 Diffusion barriers within one RuO_2(111) surface unit-cell (in eV). The different columns indicate the occupation of the third site within the surface unit-cell (empty (e), O or CO). The variation over the different columns thus reflects the lateral interactions with nearby adsorbed species.

3rd-site \ Diffusion		e	O	CO
O	$Ru_1Ru_2 \rightarrow Ru_2$	1.15	0.82	1.11
	$Ru_2 \rightarrow Ru_1Ru_2$	0.54	0.25	0.00
	$Ru_2 \rightarrow Ru_2Ru_3$	0.66	0.35	0.15
	$Ru_2Ru_3 \rightarrow Ru_2$	0.32	1.18	0.76
CO	$Ru_1Ru_2 \rightarrow Ru_2$	0.71	0.20	0.43
	$Ru_2 \rightarrow Ru_1Ru_2$	1.05	0.68	0.31
	$Ru_2 \rightarrow Ru_2Ru_3$	1.32	0.65	0.79
	$Ru_2Ru_3 \rightarrow Ru_2$	0.42	1.13	0.70

Lateral interactions in diffusion processes between sites within one surface unit-cell are equally resolved by explicitly calculating the initial and transition state for every possible occupation of the third site. This yields the total of 12 forward and 12 backward diffusion process barriers compiled in Table 5.2. The large barrier variation obtained for the same diffusion process and varying occupation of the third adsorption site reveals equally large lateral interactions as for the desorption processes. This contrasts previous findings for CO oxidation at Pd model catalysts,[126-128] where a rough scaling of initial and transition state energies rendered diffusion barriers largely independent of the local environment. As further illustrated below we attribute this difference to the much higher structural flexibility of the largely under-coordinated Ru_2 atom at RuO_2(111), which thus adapts more strongly to nearby bonded adsorbates.

For diffusion processes across surface unit-cells, i.e. from site Ru_2 in one cell to Ru_1Ru_2 in a neighboring cell, test calculations indicate only small variations of the transition state energy with varying occupation of other sites both in the original and in the destination surface unit-cells. Diffusion barriers thus essentially vary only with changes of the initial state energy, i.e. with the binding energy of the diffusing species. For both Ru_1Ru_2 and Ru_2Ru_3 sites empty in the outgoing cell, we calculate O and CO diffusion barriers of 1.25 eV and 1.87 eV, respectively. Barriers for other occupations of these

two sites are then derived by correcting these values according to the changes in the adsorbate binding energy summarized in Table 5.1.

Table 5.3 LH CO oxidation reaction barriers (in eV). The different columns indicate the occupation of the third site within the surface unit-cell (empty (e), O or CO). The variation over the different columns thus reflects the lateral interactions with nearby adsorbed species.

Reaction / 3rd-site	e	O	CO
O@Ru_1Ru_2+CO@Ru_2	0.97	1.19	0.98
CO@Ru_1Ru_2+O@Ru_2	1.02	1.01	0.71
O@Ru_2+CO@Ru_2Ru_3	1.13	1.01	0.93
CO@Ru_2+O@Ru_2Ru_3	1.70	1.20	1.11

Depending on the occupation of the third site within the surface unit-cell, there are twelve possibilities for LH-type CO oxidation reactions with CO and O sitting in nearest-neighbor sites. Table 5.3 compiles the corresponding reaction barriers, again explicitly calculated for every configuration. Also in this case, significant lateral interactions can be discerned, although at a somewhat reduced level compared to the reactant binding energetics. ER-type reactions of an impinging CO molecule can in principle occur with a surface O atom adsorbed in any of the three sites. However, when the (on average for CO most attractive, cf. Table 1) Ru_2 site is empty, our PES scans showed that adsorption into this site is more favorable compared to an ER-reaction with O atoms either at Ru_1Ru_2 or Ru_2Ru_3 sites. We therefore only consider ER-processes either with O at the Ru_2 site (calculated barrier: 0.54 eV), or with O at the other two sites whenever the Ru_2 site is occupied by O or CO. The barriers for the latter cases are then, 0.22 eV (O@Ru_1Ru_2 with CO@Ru_2), 0.49 eV (O@Ru_2Ru_3 with CO@Ru_2) and 0.42 eV (O@Ru_2Ru_3 with O@Ru_2). To fix the prefactors for the ER rate constants estimates for the sticking coefficients are required.[18] In contrast to the non-activated O_2 adsorption, these sticking coefficients have to account for the significant reduction of CO entropy when passing through the tight transition state. We specifically choose a sticking coefficient of 0.05%, which roughly corresponds to a loss of 90% of the CO gas-phase entropy at the transition state. This particular choice leads to a prefactor that is one order of magnitude higher than the one employed by Hirvi et al.,[129] who assumed a

complete loss of entropy at the transition state. As further discussed below, even with our larger prefactor the ER reaction processes do not play a significant role around ambient pressure conditions and 600 K. In fact, for this to happen, the prefactor would need to be increased by another 1-2 orders of magnitude. For the present purposes the uncertainty in the ER prefactor is therefore not problematic. Future work will, however, aim for a more precise determination of prefactors for ER reactions in general, as we find the contribution of ER reactions increased at lower temperatures.

5.2.3 1p-kMC simulation setup

All 1p-kMC simulations are carried out with the kmos framework.[87] We employ a simulation cell comprising (20x20) surface unit-cells and periodic boundary conditions. Test simulations involving larger lattices produced identical average steady-state coverages and TOFs. Simulations are run for fixed (T,p_{O2},p_{CO})-conditions. After an initial equilibration period, steady-state values are obtained as long-time averages over 5 x 10^8 1p-kMC steps. The obtained steady states were always found to be independent from the initial starting configuration.

5.3 Results and discussion

5.3.1 CO and O adsorption geometries and energetics

At the surface, Ru atoms can exhibit new electronic configurations due to a reduction of their sixfold O coordination in rutile bulk. Specifically, the O-poor RuO_2(111) surface termination used as basis for our 1p-kMC approach exhibits two types of fivefold coordinated surface Ru atoms (Ru_1 and Ru_3) and one threefold coordinated surface Ru atom (Ru_2) per surface unit-cell, cf. Fig. 5.1. In comparison, the analogue O-poor termination used in previous such work for the RuO_2 (110) surface[18, 45, 85, 118] has two symmetry-equivalent fourfold coordinated surface Ru atoms (Ru_{br}) and one fivefold coordinated surface Ru atom (Ru_{cus}) per surface unit-cell. Identifying similarities and differences for O and CO adsorption at these under-coordinated sites forms a general basis for an analysis of a possible structure sensitivity[120-121] of the CO oxidation

reaction. At oxide surfaces it is furthermore instructive in view of relations to homogeneous catalysis at metal complexes.[130]

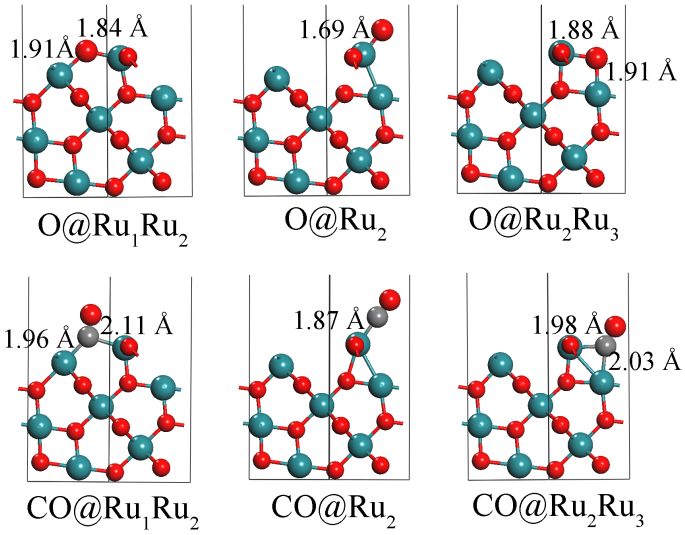

Figure 5.2 Side views of the adsorption geometries of O (upper panels) and CO (lower panels) at the three adsorption sites (Ru_1Ru_2, Ru_2, Ru_2Ru_3) offered by the O-poor $RuO_2(111)$ termination used as basis for the 1p-kMC approach. Ru atoms are shown as large blue spheres, O atoms as small red spheres, and C atoms as small gray spheres.

Figure 5.2 summarizes the calculated adsorption geometries of O and CO at the three different $RuO_2(111)$ binding sites. This immediately reveals that a classification of adsorption properties merely based on the level of under-coordination of the involved metal center falls short at the extended surfaces. At the $RuO_2(110)$ surface, both O and CO adsorption at the fivefold coordinated Ru_{cus} atoms occurs in an atop position, with only one predominant adsorbate-substrate bond formed.[13-14, 83, 100, 131] In contrast, at $RuO_2(111)$ both fivefold coordinated Ru_1 and Ru_3 atoms yield to bridge-type adsorption geometries that also involve the adjacent threefold coordinated Ru_2 atom. The O and CO bonding at the resulting Ru_1Ru_2 and Ru_2Ru_3 sites may therefore rather bear similarities to the equally bridge-type O and CO bonding at the fourfold coordinated Rubr atoms of the $RuO_2(110)$ surface. The Ru-O bond lengths shown in Fig. 5.2 are indeed more comparable in this respect. They are 1.69 Å at the Ru_2 site and in the range 1.84–1.91 Å at both Ru_1Ru_2 and Ru_2Ru_3 sites. This contrasts with 1.70 Å for atop Ru_{cus}-O and 1.91 Å for bridge Ru_{br}-O.[14, 131] In the case of CO this translates to bond lengths of 1.87 Å at the Ru_2 site and 1.96 – 2.11 Å at Ru_1Ru_2 and Ru_2Ru_3 vs. 1.95 Å for atop Ru_{cus}-CO and 1.99 – 2.06 Å for bridge Ru_{br}-CO.[83] The strong asymmetry in the

bridge site adsorption at RuO_2(111) is thereby likely caused by the coordination to one fivefold (Ru_1,Ru_3) and one threefold (Ru_2) coordinated Ru atom. However, an asymmetric adsorption geometry has also been reported for high-coverage CO_{br} adsorption in the bridge site coordinating to the two symmetry-equivalent Ru_{br} atoms.[132] The geometric classification in terms of site-type rather than degree of under-coordination of the involved Ru atom(s) also carries over to the atop-type adsorption of O and CO at the Ru_2 site. Here, the bond lengths shown in Fig. 5.2 compare very well to the equivalent ones for atop adsorption at Ru_{cus} atoms, despite the differences in the Ru_{cus} (fivefold) and Ru_2 (threefold) coordination.

Table 5.4 O binding energy (in eV) at the three RuO_2(111) adsorption sites. The different columns indicate the occupation of the other two sites within the surface unit-cell (empty (e), O or CO). The variation over the different columns thus reflects the lateral interactions with nearby adsorbed species.

O binding energy									
	e e	e O	e CO	O e	O O	O CO	CO e	CO O	CO CO
O@Ru_1Ru_2	-2.32	-2.41	-2.83	-1.24	-1.45	-1.21	-1.45	-1.83	-2.09
O@Ru_2	-1.71	-1.84	-1.72	-0.63	-0.88	-0.10	-0.64	-1.18	-0.02
O@Ru_2Ru_3	-1.37	-1.50	-1.39	-1.46	-1.71	-1.77	-1.25	-1.79	-1.31

Proceeding to the adsorption energetics Tables 1 and 4 compile the calculated CO and O binding energies at the three adsorption sites, respectively. These energies exhibit a large variation of in parts up to almost 2 eV depending on the occupation of the other two sites in the surface unit-cell. The thereby implied strong lateral interactions prohibit any clear-cut qualitative distinction of the three adsorption sites. This is in strong contrast to the RuO_2(110) surface, where only small to negligible lateral interactions below ~0.2 eV were found between adsorbates at the two prominent adsorption sites.[18, 45, 83] We attribute this difference primarily to the high structural flexibility of the highly under-coordinated Ru_2 atom in comparison to the more rigid arrangement of the under-coordinated Ru atoms in the less open RuO_2(110) surface. Depending on the occupation of the nearby adsorption sites we calculate maximum displacements of the Ru_2 atom of up to 0.80 Å away from its relaxed position at the clean surface termination. These large relaxations are also apparent in the calculated adsorption geometries

shown in Fig. 2 and contrast maximum relaxations calculated for the Ru_{br} and Ru_{cus} atoms at RuO_2(110) of the order of 0.1-0.2 Å.[14, 18, 83, 131-132]

In case of the RuO_2(110) surface the small lateral interactions allowed to unambiguously distinguish in particular between O adsorption at Ru_{br} (binding energy: ~2.4 eV [18, 83]) and at Ru_{cus} (binding energy: ~1 eV [18, 83]). With a too strong O adsorption at Ru_{br}, this then immediately pointed at a prominent role of the cus site for steady-state CO oxidation at near-ambient and near-stoichiometric feed conditions.[13, 100] Such a fingerprinting is not possible for the three RuO_2(111) sites. It would not even be possible on the basis of the actually calculated LH CO oxidation reaction barriers, cf. Table 3. Intriguingly, these barriers exhibit significantly smaller variations with the occupation of the third adsorption site than the concomitant reactant binding energies. This shows that approximate treatments of lateral interactions applied successfully at other surfaces[126-128] would not work at RuO_2(111) and an explicit full calculation as done here is required. Nevertheless, despite these smaller variations in the reaction barriers it is still not a priori obvious which reaction mechanism could possibly dominate the catalytic activity. Even more as at surfaces without such strong lateral interactions, this dictates to explicitly evaluate the interplay of the elementary processes within a microkinetic model in order to capture and analyze the catalytic function of this surface.

With respect to structure sensitivity, this data already indicates that the spatial arrangement of the active sites is another crucial factor for oxide catalysis that leads to a structure sensitivity of a reaction. Intriguingly, even in a hypothetical “low-coverage” limit, i.e. in the absence of lateral interactions, the calculated binding energies and reaction barriers reveal a structure sensitivity of the CO oxidation reaction at RuO_2(111). Despite the afore discussed similarity in the bonding geometries at the bridge-type and atop-type sites, the O and CO binding energies at like sites at the RuO_2(110) and RuO_2(111) surfaces do not compare, cf. columns ee without neighboring adsorbates in Tables 5.1 and 4 for RuO_2(111) with the above quoted binding energies at RuO_2(110) br and cus sites. Since the same adsorption site types (br, atop) at RuO_2(110) and RuO_2(111) involve differently coordinated surface Ru atoms, one could try to attribute this difference to an electronic effect arising from the differing degree of undercoordination[120]. However, even the O and CO binding energies at the Ru_1Ru_2 and Ru_2Ru_3 sites themselves differ by ~1 eV and ~0.6 eV, respectively. Both sites have an

equivalent geometry (bridge) and electronic configuration (coordination to one threefold and one fivefold coordinated Ru atom). This demonstrates that the concepts that have been put forward to classify structure sensitivity at metal catalysts[120] cannot be carried over to these oxide surfaces.

5.3.2 Coverage and turnover frequency at catalytically active conditions

We concentrate our analysis of the catalytic function on a reaction temperature of 600 K, which lies at the upper range of interest for CO oxidation. This temperature was also specifically studied in the previous 1p-kMC work at RuO_2(110)[18, 45, 85, 118], which then enables the detailed comparison targeted here.

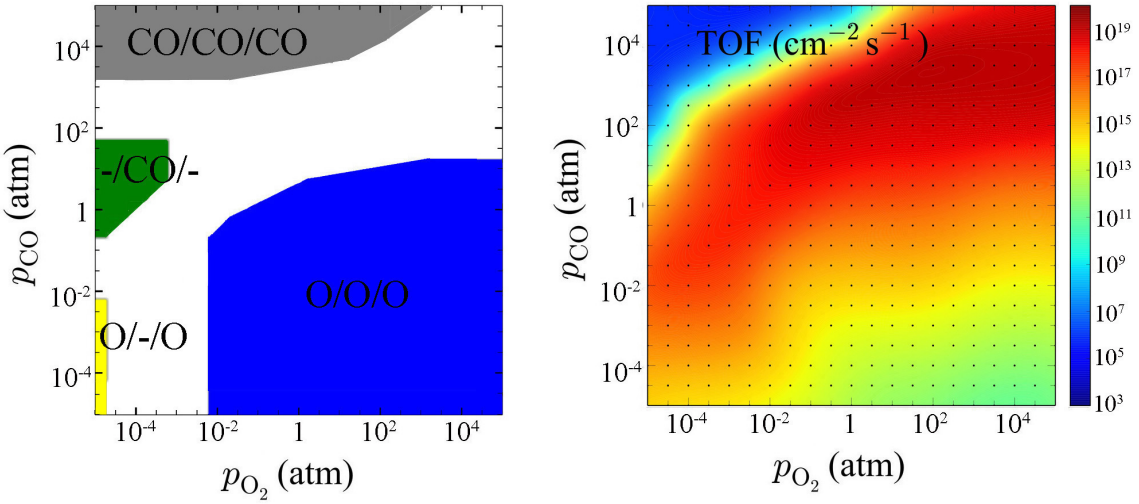

Figure 5.3 1p-kMC computed steady-state O and CO surface coverage (left panel) and CO turnover frequency, TOF (right panel). Shown are data for a range of CO and oxygen partial pressures at 600 K. The short-hand notation for the various differently colored coverage phases in the left panel indicates the dominant species (O, CO, or empty '–') at the three sites offered by the RuO_2(111) surface, e.g. O/O/O indicates a steady-state O coverage >80% at sites Ru_1Ru_2/Ru_2/Ru_2Ru_3. White regions between the colored phases indicate coexistence of species at least at one of the three sites.

Figure 5.3 displays the 1p-kMC calculated steady-state average surface coverages and CO oxidation TOFs over a range of reaction partial pressures around ambient conditions. At the lowest p_{CO}~10^{-5} atm shown the catalytic activity starts to die out and the surface coverages obtained as a function of oxygen pressure necessarily agree with those obtained within the constrained *ab initio* thermodynamics approach,[14, 83, 131] which

neglects any kinetic effects of ongoing catalytic reactions on the surface composition. The correspondingly calculated surface phase diagram is shown in Fig. 5.4 and equally exhibits a transition between a phase where the Ru_1Ru_2 and Ru_2Ru_3 sites are covered with oxygen atoms (denoted as O/–/O) and a fully O-covered surface (denoted as O/O/O). Within the constrained *ab initio* thermodynamics approach configurational entropy is neglected. The phase transition is therefore infinitely sharp, whereas the 1p-kMC simulations fully account for the temperature-induced widening of the transition over a finite range of oxygen pressures.[18, 45, 119]

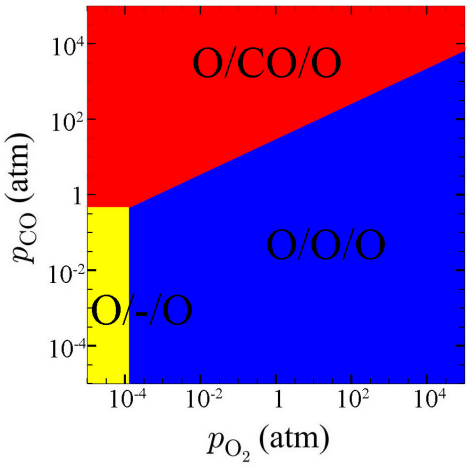

Figure 5.4 Steady-state coverage map as obtained from constrained *ab initio* thermodynamics. The nomenclature for the different phases is the same as in the left panel of Fig. 5.3.

At increasing CO pressures catalytic activity sets in. The higher CO impingement increases the probability for ER reactions and enables LH reactions due to the increased stabilization of CO at the surface. As shown in Fig. 5.4, from a thermodynamic point of view this stabilization should notably set in close to ambient CO pressures at low p_{O2}. With increasing oxygen pressures correspondingly higher p_{CO} are then required to lead to the corresponding O/CO/O phase, in which CO predominantly covers the Ru_2 sites. Comparing these predictions to the actual 1p-kMC results in Fig. 5.3 we indeed start to find a significant CO concentration at the surface in this pressure range. Also, the thermodynamically intuitive shift of the corresponding coexistence range (depicted as a white region in Fig. 5.3) to higher p_{CO} with increasing p_{O2} is obtained. However, strong kinetic effects lead to a completely different surface composition as anticipated by the approximate constrained *ab initio* thermodynamics theory. While the dominant CO coverage at the Ru_2 site is retained, these kinetic effects strongly suppress the presence of oxygen at the Ru_1Ru_2 and Ru_2Ru_3 sites. Instead of

the thermodynamically predicted O/CO/O phase, these two sites are thus either largely empty (the region denoted –/CO/– in Fig. 5.3) or at higher p_{CO} largely covered with CO (the CO/CO/CO region in Fig. 5.3). The consideration of the kinetic effects on the surface population due to the ongoing CO oxidation reactions therewith leads to a much earlier CO poisoning of the surface with increasing CO pressures. This finding was analogously obtained in the earlier work on the RuO_2(110) surface; compare specifically with the CO_{br}/– and CO_{br}/CO_{cus} regions in the upper left part of Fig. 5.3 in Ref. [18], which is completely equivalent to the present Fig. 5.4 for RuO_2(111). Here and there, the central reason for this strong suppression of surface O species at corresponding high CO partial pressures are the kinetic limitations in finding two adjacent empty sites required for the dissociative O_2 adsorption at the highly covered surfaces.[118]

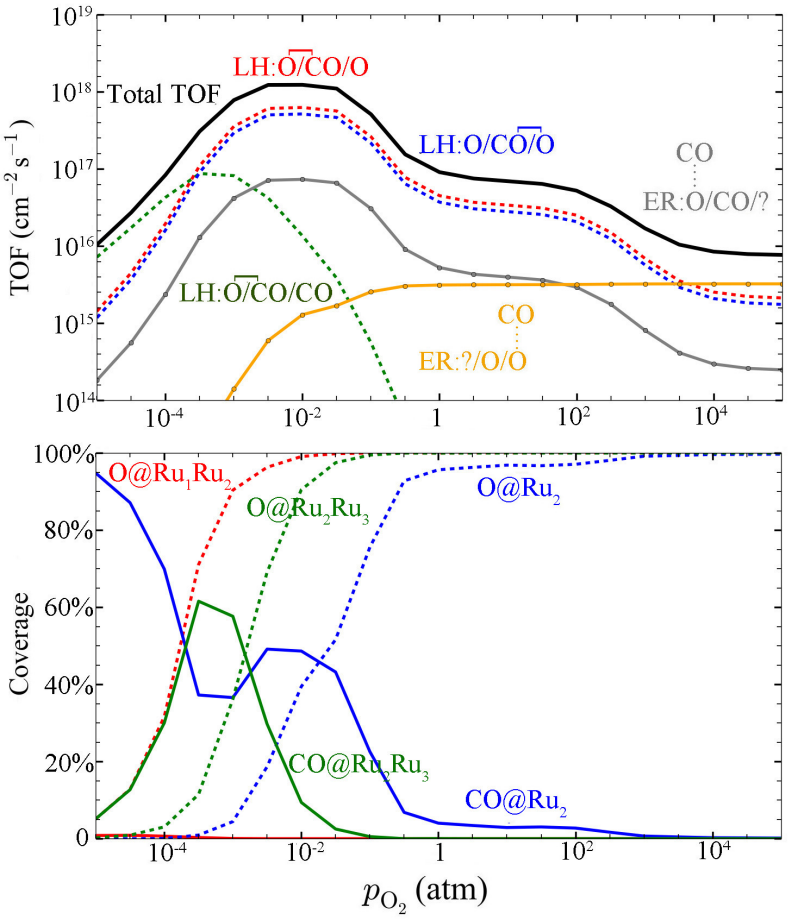

Figure 5.5 1p-kMC computed steady-state turnover frequency, TOF (upper panel), and surface coverages (lower panel) at p_{CO} = 1 atm and 600 K. In addition to the total TOF, the individual contributions from different reaction mechanisms are shown as colored lines. The employed short-hand notation indicates the predominant coverage at the three sites as in Figs. 5.3 and

5.4, with a bracket above two sites indicating the two reaction intermediates involved in LH reactions, and a CO atop one of the sites indicating which O adsorbate is picked up in ER reactions.

Corresponding pressure regions in the upper left part of Fig. 5.3 which presently yield CO-rich surface compositions are in reality prone to lead to further oxide reduction. This is not possible in the present 1p-kMC model which focuses on the surface adsorption sites at an otherwise intact oxide surface. In the following we therefore rather concentrate on relatively lower CO pressures, where at least for sufficiently large p_{O2} Fig. 5.3 predicts an appreciable concentration of surface O species and where we would therefore at least expect a metastability of the underlying oxide matrix. Specifically, Fig. 5.5 shows the detailed surface coverages and TOF contributions of individual reaction mechanism for p_{CO} = 1 atm and varying oxygen pressures. The peak activity obtained for these conditions is about one order of magnitude lower than the peak activity observed for RuO_2(110), which was 4 x 10^{19} $cm^{-2}s^{-1}$.[18, 85] It is 1 x 10^{18} $cm^{-2}s^{-1}$ along the plotted line of p_{CO} = 1atm in Fig. 5. The overall maximum activity for the RuO_2(111) facet at 600 K is 6 x 10^{19} $cm^{-2}s^{-1}$ in Fig. 5.3, which is thus almost identical to the peak activity of RuO_2(110).

The two dominantly contributing mechanisms to this peak activity are the LH mechanisms O@Ru_1Ru_2 + CO@Ru_2 (with O@Ru_2Ru_3, barrier: 1.19 eV) and O@Ru_2Ru_3 + CO@Ru_2 (with O@Ru_1Ru_2, barrier: 1.20 eV). At the pressures corresponding to this peak activity, these two mechanisms benefit mostly from the prevalent surface composition, which is characterized by a coexistence of oxygen and CO at the Ru_2 and Ru_2Ru_3 sites, with O atoms already predominantly present at the Ru_1Ru_2 sites (white coexistence region in Fig. 5.3). ER reactions do not contribute significantly to the peak activity. They only start to take over at very high oxygen pressures, cf. Fig. 5.5. At these extremely oxygen-rich conditions the surface is completely oxygen poisoned (O/O/O phase). The concomitantly low surface CO concentration then effectively suppresses any of the LH mechanisms. This increased contribution of ER processes to the total TOF at high p_{O2} leads to the rather weak decline of the catalytic activity towards the right in the TOF-map of Fig. 5.3. This contrasts the plummeting TOFs for increasing p_{O2} obtained in the previous 1p-kMC work on RuO_2(110), where ER processes were not considered.[18, 45, 85] Whether the latter works need to be revised in this respect, or whether the current ER contribution is

overestimated depends critically on the employed prefactor in the corresponding first-principles rate constants. Compared to the work of Hirvi et al.[129] the estimate used in this work is an upper bound and even then ER processes do not play a role for the near-ambient peak activity at 600 K.

Similar to the case for RuO_2(110)[18, 83] it is thus by far not the LH mechanisms that exhibit the lowest reaction barriers that dominate the catalytic peak activity around ambient pressures. In principle the RuO_2(111) surface would exhibit mechanisms with barriers even about 0.5 eV lower, cf. Table 5.3. Yet, they cannot contribute in the interplay of all elementary processes, which underscores the importance of the explicit evaluation of this interplay within a microkinetic model. Interestingly, the shortcoming of individual energy barrier values to predict catalytic activity extends also to the comparison of the two RuO_2 facets. The two dominant reaction mechanisms at RuO_2(111) exhibit barriers that are about 0.3 eV higher than the barrier of the dominant reaction mechanism at the RuO_2(110) surface (O_{cus} + CO_{cus}, 0.8 eV [18, 83]). In a naïve Arrhenius picture and with RuO_2(110) and RuO_2(111) exhibiting approximately equal site densities per area one would then expect the two peak catalytic activities to differ by ~exp (-0.3 eV / kBT) ≈ 10^{-3} at 600K. In contrast, the explicit 1p-kMC simulations yield virtually identical peak activities. In addition to the differing absolute TOF value, the computed peak activity of RuO_2(111) occurs furthermore at different partial pressure ratios than the one at RuO_2(110). For the p_{CO} = 1atm condition in Fig. 5.5 it is obtained at p_{O2} = 6.8 x 10^{-3} atm, i.e. for a partial pressure ratio of p_{CO}/p_{O2} ~ 150. In contrast, for RuO_2(110) at corresponding near-ambient total pressures it was obtained for a partial pressure ratio of p_{CO}/p_{O2} ~ 5.[18] The catalytic activity of the RuO_2(111) surface extends therefore much more to reducing feed conditions. This is fully consistent with recent experimental reports of a preferential reduction of the apical RuO_2(111) facets of RuO_2 crystals in reducing feeds.[98]

Finally, we return again to the exceeding similarity of the peak activities found for RuO_2(110) and RuO_2(111) at 600 K. First of all, this is already surprising in view of the differences in the elementary processes and their rate constants discussed in Section 5.3.1. It is even more surprising when considering the two quite different reasons why the catalytic activity at the two RuO_2 facets cannot be captured with prevalent mean-field kinetic models. At RuO_2(110) this arises out of a strong binding of oxygen at the br

adsorption sites,[18, 83] which restricts the catalytic activity primarily to the remaining cus sites. Even though there are only insignificant lateral interactions between reaction intermediates at these sites, the row-like arrangement of the cus sites together with concomitant diffusion limitations in the resulting one-dimensional cus-trenches then lead to the non-random spatial distribution of the reaction intermediates that causes the break-down of the mean-field assumptions.[85, 118] In contrast, at RuO_2(111) there is no extended site network, but instead independent tri-site clusters to which the essential elementary processes are confined. Among this group of sites it is then strong lateral interactions that leads to site occupation and activity patterns that are beyond the reach of mean-field kinetics.

In view of these qualitative differences in the site arrangement, interplay of elementary processes and even the underlying individual elementary processes, CO oxidation at these two RuO_2 facets appears as a structure sensitive reaction par excellence. In this respect, the almost identical peak activity albeit at differing partial pressure ratios has another important implication. For partial pressure ratios $5 < p_{CO}/p_{O2} < 50$, i.e. in between the limits where one or the other facet exhibits its peak activity at near-ambient pressures, both facets correspondingly exhibit somewhat smaller, but still high activity. Precisely for such partial pressure ratios that are most relevant for practical catalysis and that are concomitantly typically explored in experimental studies, we can therefore easily find multiple absolute pressure conditions where both facets again exhibit identical TOFs. This should be seen with respect to the traditional classification or definition of a reaction as structure insensitive based merely on the macroscopically observed catalytic function as typically explored only over a small set of feed conditions.[113-116] As exemplified by the data obtained here for RuO_2(111) and RuO_2(110) this can be a dangerous concept that does not adequately capture the underlying micro- to mesoscopic complexities. We stress, however, that this is a general statement based on the well-defined theory-theory comparison of the two 1p-kMC models of RuO_2(110) and RuO_2(111). For Ru nanoparticles in oxidizing feeds Hoon Joo et al.[133] in fact reported a structure sensitivity for the CO oxidation reaction, which they, however, ascribed to a varying degree of oxidation with nanoparticle size.

5.4 Conclusions

We presented a 1p-kMC study of CO oxidation at RuO_2(111) and compared the obtained detailed data on the adsorption energetics and geometry, as well as surface composition and catalytic activity under steady-state reaction conditions with corresponding data available for the RuO_2(110) facet. This comparison provides detailed insights into the structure sensitivity of this reaction and on the catalytic function of RuO_2 nanoparticles. In terms of under-coordinated surface Ru atoms both facets share similarities at first sight. A more detailed inspection of the adsorption sites reveals, however, that the bonding of the reaction intermediates at the fivefold coordinated Ru atoms present at both surfaces is qualitatively different. Some structural similarity can instead be discerned on the level of similarly coordinated adsorption sites, in particular bridge-type sites present at both facets. Notwithstanding, even at these sites the adsorbate binding energetics is largely different, which shows that the understanding of structure sensitivity in terms of geometric and electronic factors that has been developed for metal catalysts does not carry over to these oxide surfaces. This even more so, as at RuO_2(111) the presence of a structurally most flexible, only threefold coordinated surface Ru atom leads to strong lateral interactions. These interactions in fact prevent any straightforward identification of particularly ‘active’ sites – a concept that has been so successfully applied for the ‘cus’-sites of the extensively studied RuO_2(110) surface.

Also on the level of the spatial arrangement of the individual adsorption sites both facets exhibit qualitative differences. At RuO_2(111) the three adsorption sites situated within one surface unit-cell are largely decoupled from sites in neighboring cells. This together with the strong lateral interactions between adsorbates at the three clustered sites yields a molecular-type catalytic behavior that cannot be grasped with prevalent mean-field microkinetic models. In contrast, at RuO_2(110) only very modest lateral interactions seemingly suggest the applicability of mean-field approaches. Here, however, the strong O binding at one of the two adsorption site types largely poisons the corresponding sites at near-stoichiometric feeds, which then leads to a micropatterning of the surface. In consequence, the catalytic reactions run prominently along one-dimensional trenches, which – again – is beyond the reach of mean-field kinetics.

Despite all of these differences, at 600 K the peak activity of both facets is virtually identical. The underlying surface coverages and concomitant reaction patterns are

thereby quite different though. With the surface composition varying differently with reactant pressures, the peak activity of the two facets is correspondingly obtained at different partial pressure ratios. Already the data obtained for these two RuO_2 facets thus suggests that the concept of one set of 'optimum reaction conditions' is generally short-sighted for catalyst nanoparticles. For near-ambient pressures and near-stoichiometric feeds both facets exhibit slightly lower activities compared to their respective peak activities. Intriguingly, these activities are, however, again exceedingly similar to each other. Probing the catalytic activity only for a restricted set of gas-phase conditions in this range would therefore erroneously suggest the reaction to be structure insensitive – at least according to the prevailing macroscopic definition of structure sensitivity.

At the elevated temperature analyzed in this study, the peak activity of RuO_2(111) is shifted to lower O_2 pressures compared to RuO_2(110). This seems consistent with recent experimental reports pointing at a prominent role of these apical facets in the reduction of RuO_2 crystals at elevated temperatures. As to the long-term steady-state activity, the obtained different composition and activity patterns of the two studied facets hint at interesting mass transport effects over the facet edges of RuO_2 nanoparticles. These will be the focus of ensuing work along our long-term track of systematically bridging between single-crystal model and real catalysis.

6

Summary and outlook

The CO oxidation reaction has been extensively used as a ‘simple’ model reaction to push our molecular-level understanding of heterogeneous catalysis. This concerns in particular model catalyst studies on low-index single-crystal surfaces. For such systems often close agreement between detailed measurements and quantitative theoretical modeling can be achieved. Unfortunately, the situation is much less advanced for ‘real’ catalyst particles. This is prototypically reflected by the situation for RuO_2, as a most active catalyst for CO oxidation. Here, existing first-principles kinetic modeling is restricted to just one facet, namely the RuO_2(110) surface. In order to close the gap to detailed measurements at RuO_2 powder catalysts, we focus in this thesis on extending this RuO_2(110)-centered knowledge. We studied the surface structure and composition of among others the relevant (100), (101) and (111) facets of RuO_2 in oxygen gas-phases ranging from UHV up to technologically relevant conditions, using state-of-the-art DFT calculations combined with thermodynamic considerations. In view of the existing experimental evidence, this comprised the development of structural models for O-deficient, stoichiometric and O-rich terminations as initial steps to elucidate the observed deactivation and reduction of the oxide catalyst. Simultaneously, we used the obtained detailed surface energetic data to arrive at a first estimate of the overall crystal shape by means of a Wulff-construction.

The obtained equilibrium shape of RuO_2 particles in an oxygen environment is fully consistent with the different crystal shapes reported for different calcination pretreatments in recent powder catalyst studies,[22, 25, 98] except for the fact that the experimental particles are much more columnar than the first-principles Wulff shapes. For the higher-temperature calcination used by Rosenthal et al.,[22, 98] we attribute this to a microfacetting of the lateral facets, RuO_2(110) and RuO_2(100), into inactive c(2x2)-RuO_2(100) which is not contained in the present model. For the lower-temperature calcination used by Narkhede et al.,[25] this rather points towards an incomplete shape equilibration in the pretreatment. This strongly suggests revisiting the morphology–activity relationship for high chemical potential calcination. If the first-principles Wulff shape is validated, this could yield a new type of active RuO_2 catalyst with long-term stability in oxidizing feed. Our results generally indicate a sensitive dependence of the crystal habit on the O chemical potential: Different oxidizing pretreatments are found to critically affect the crystal habit by changing the cross section from quadratic to octagonal, as well as the share and type of facets exposed. Correlating the reported

initial activities towards CO oxidation in oxidizing feed with this detailed insight about the crystal habit supports the interpretation of Rosenthal et al.[22, 98] in terms of a prominent role of the hitherto little studied {101} and {111} apical facets.

Enlightened by this first part of our work, we performed a 1p-kMC simulation of CO oxidation at RuO_2(111) and compared the results with RuO_2(110) in terms of adsorption energetics and geometry, as well as surface composition and catalytic activity under steady-state reaction conditions. This comparison provides detailed insights into the structure sensitivity of this reaction and on the catalytic function of RuO_2 nanoparticles. At first sight, both facets share similarities in terms of under-coordinated surface Ru atoms, i.e. the fivefold coordinated Ru atoms. However, the bonding of the reaction intermediates on these adsorption sites is qualitatively different. For these similarly coordinated adsorption sites, in particular bridge-type sites, both surfaces show some similarity on bonding structures, but very different binding energetics. This suggests that the understanding of structure sensitivity in terms of geometric and electronic factors that has been developed for metal catalysts does not carry over to these oxide surfaces. More specifically, there is an only threefold coordinated surface Ru atom at RuO_2(111). This threefold Ru leads to strong lateral interactions, which prevents any straightforward identification of particularly ‘active’ sites – a concept that has been so successfully applied for the ‘cus’-sites of the extensively studied RuO_2(110) surface.

Despite the differences discussed above, both facets also exhibit qualitative differences on the level of the spatial arrangement of the individual adsorption sites. At RuO_2(111), there is almost no lateral interaction between adsorbates at sites in neighboring cells, but quite strong lateral interactions at the three adsorption sites within one surface unit-cell. This yields a molecular-type catalytic behavior, which cannot be grasped with prevalent mean-field microkinetic models. In contrast, at RuO_2(110) only very modest lateral interactions seemingly suggest the applicability of mean-field approaches. However, at near-stoichiometric feeds, one of the two adsorption sites gets largely O poisoned due to the strong O binding, leading to a micro-patterning of the surface. As a consequence, the catalytic reactions run prominently along one-dimensional trenches, which also is beyond the reach of mean-field kinetics.

Although both facets thus exhibit large differences in many respects, both facets show virtually identical peak activities at 600 K. The peak activity of RuO_2(111) is thereby shifted to lower O_2 pressures compared to RuO_2(110) at this elevated temperature. This is consistent with recent experimental reports, which point at a prominent role of these apical facets in the reduction of RuO_2 crystals at elevated temperatures. At partial pressure ratios slightly off from those corresponding to the peak activities, the surface composition and the underlying reaction patterns are quite different. Nevertheless, both facets exhibit only slightly lower activities compared to their respective peak activities at near-ambient pressures and near-stoichiometric feeds. Intriguingly, these activities are again exceedingly similar to each other. According to the prevailing macroscopic definition of structure sensitivity, if only probing the catalytic activity for a restricted set of gas-phase conditions in this range, the reaction would erroneously be classified as structurally insensitive. The different gas-phase conditions for which either of the two facets exhibits its peak activity furthermore reveals that the concept of one set of 'optimum reaction conditions' is generally short-sighted for catalyst nanoparticles.

In summary, our work has established important insight into the CO oxidation at RuO_2 particles, in particular into the crystal shape behavior during the induction period and possible avenues to the deactivation mechanism. The detailed insight provided by the obtained Wulff construction allowed us to focus our kinetic modeling on the relevant (111) facets. The direct comparison of the detailed activity and structural insight with the (110) facet then allowed for an in-depth discussion towards the differences between the catalytic properties of the individual single-crystal surfaces, significantly contributing to the general understanding of structure sensitivity, e.g. through the relation of binding properties of differently coordinated Ru surface atoms and the obtained TOFs. These findings challenge the traditional definition of structure sensitivity based on macroscopically observable turnover frequencies and allow to scrutinize the applicability of structure sensitivity classifications developed for metals to oxide catalysis.

The above success motivates further studies on the following aspects. First of all, it is necessary to fully unravel the explicit structure of the RuO_2(100)-c(2x2) reconstruction and therewith the deactivation mechanism. Secondly, a detailed study of the activity of RuO_2(111) at lower temperatures for which an improved estimate for the prefactor for Eley-Rideal type of reactions is required. Probably a MD simulations to determine the

impingement ratio of CO on the surface is needed. Last but not least, as to the long-term steady-state activity, the obtained different composition and activity patterns of the RuO_2(110) and RuO_2(111) facets hint at interesting mass transport effects over the facet edges of RuO_2 nanoparticles. Such studies would then establish a comprehensive approach to CO oxidation at RuO_2 nanoparticles, significantly advancing the state-of-the-art in the field.

7

Appendix

Co-adsorption configurations of O and/or CO on $RuO_2(111)$

To evaluate the explicit lateral interactions of adsorbents within (1x1) unit cell of $RuO_2(111)$ and setup the phase diagram of this facet in a constrained equilibrium with an oxygen and CO in gas phase, we calculated all the possible O and/or CO co-adsorption configurations, shown in the following figures. Here Ru atoms are shown as large blue spheres, O atoms as small red spheres, and C atoms as small grey spheres. We use a short-hand notation indicating the adsorption species (O, CO or empty '-') at the three sites offered by the $RuO_2(111)$ surface, e.g. O/O/O indicates O adsorbing on sites $Ru_1Ru_2/Ru_2/Ru_2Ru_3$. ΔE gives out the energy difference between the co-adsorption configuration to that of the clean surface and the corresponding adsorbents in gas phase.

1) 2O:

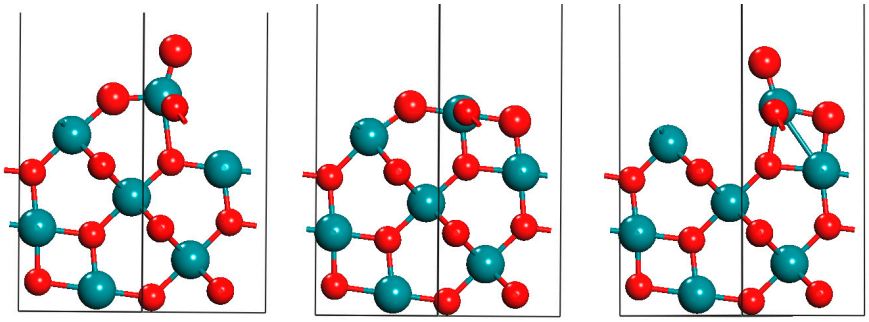

O/O/- ΔE = -2.95 eV | O/-/O ΔE = -3.78 eV | -/O/O ΔE = -3.21 eV

2) 2CO:

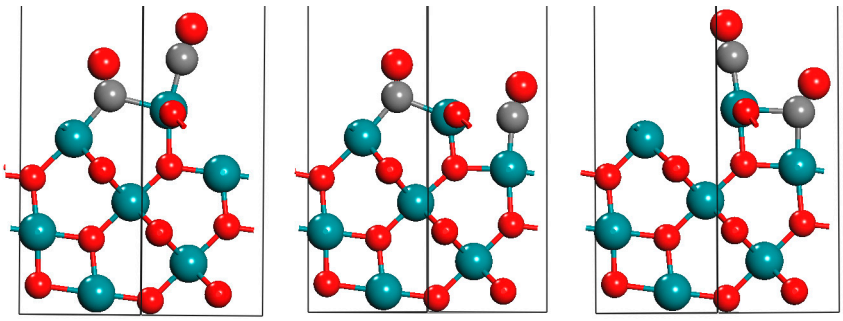

CO/CO/- ΔE = -2.78 eV | CO/-/CO ΔE = -2.69 eV | -/CO/CO ΔE = -2.57 eV

3) 1O and 1CO:

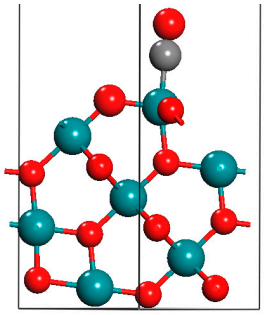

O/CO/-
ΔE = -3.33 eV

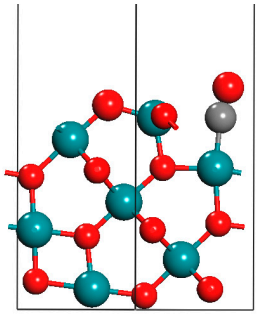

O/-/CO
ΔE = -3.81 eV

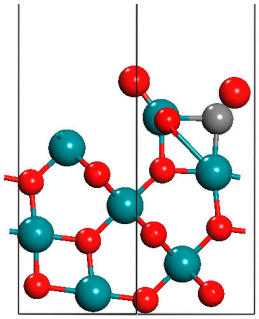

-/O/CO
ΔE = -2.70 eV

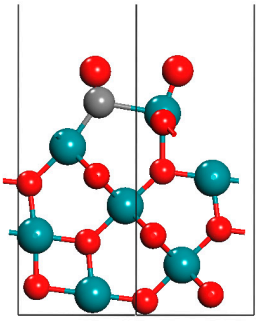

CO/O/-
ΔE = -2.18 eV

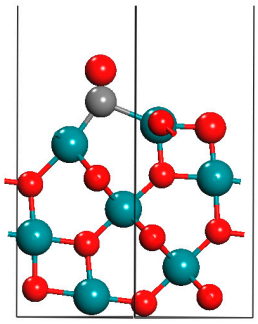

CO/-/O
ΔE = -2.79 eV

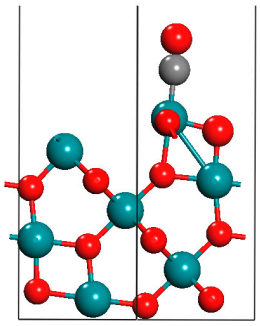

-/CO/O
ΔE = -3.27 eV

4) 1O and 2CO:

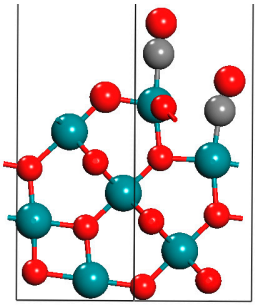

O/CO/CO
ΔE = -4.66 eV

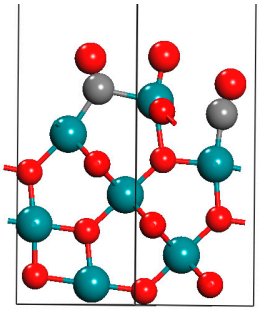

CO/O/CO
ΔE = -2.71 eV

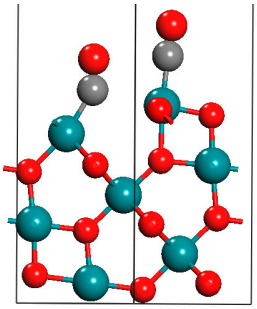

CO/CO/O
ΔE = -4.09 eV

5) 2O and 1CO:

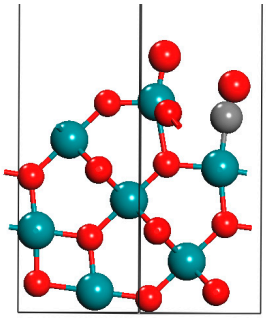

O/O/CO
ΔE = -3.91 eV

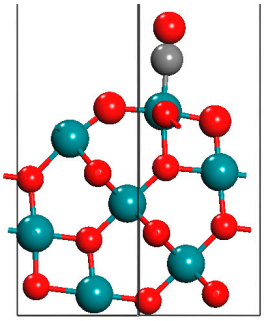

O/CO/O
ΔE = -5.10 eV

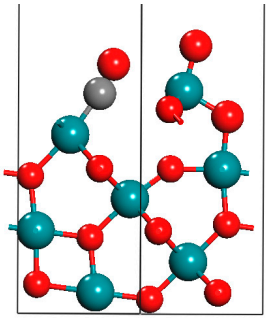

CO/O/O
ΔE = -3.97 eV

6) 3O:

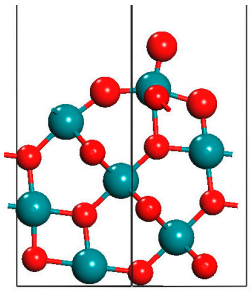

O/O/O
ΔE = -4.66 eV

7) 3CO:

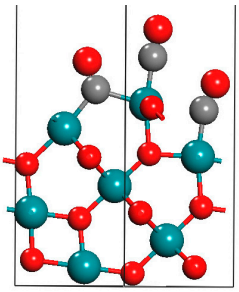

CO/CO/CO
ΔE = -3.61 eV

8

References

1. Goodman, D. W.; Peden, C. H. F.; Chen, M. S., CO oxidation on ruthenium: The nature of the active catalytic surface. *Surf. Sci.* **2007,** *601* (19), L124-L126.

2. Over, H.; Muhler, M.; Seitsonen, A. P., Comment on “CO oxidation on ruthenium: The nature of the active catalytic surface” by D. W. Goodman, C. H. F. Peden, M. S. Chen. *Surf. Sci.* **2007,** *601* (23), 5659-5662.

3. Goodman, D. W.; Peden, C. H. F.; Chen, M. S., Reply to comment on “CO oxidation on ruthenium: The nature of the active catalytic surface” by H. Over, M. Muhler, A. P. Seitsonen. *Surf. Sci.* **2007,** *601* (23), 5663-5665.

4. Peden, C. H. F.; Goodman, D. W., Kinetics of carbon monoxide oxidation over ruthenium(0001). *J. Phys. Chem.* **1986,** *90* (7), 1360-1365.

5. Todorova, M.; Lundgren, E.; Blum, V.; Mikkelsen, A.; Gray, S.; Gustafson, J.; Borg, M.; Rogal, J.; Reuter, K.; Andersen, J. N.; Scheffler, M., The Pd(100)–($\sqrt{5}\times\sqrt{5}$) R27°-O surface oxide revisited. *Surf. Sci.* **2003,** *541* (1–3), 101-112.

6. Böttcher, A.; Niehus, H.; Schwegmann, S.; Over, H.; Ertl, G., CO Oxidation Reaction over Oxygen-Rich Ru(0001) Surfaces. *J. Phys. Chem. B* **1997,** *101* (51), 11185-11191.

7. Cant, N. W.; Hicks, P. C.; Lennon, B. S., Steady-state oxidation of carbon monoxide over supported noble metals with particular reference to platinum. *J. Catal.* **1978,** *54* (3), 372-383.

8. Over, H.; Kim, Y. D.; Seitsonen, A. P.; Wendt, S.; Lundgren, E.; Schmid, M.; Varga, P.; Morgante, A.; Ertl, G., Atomic-Scale Structure and Catalytic Reactivity of the RuO_2(110) Surface. *Science* **2000,** *287* (5457), 1474-1476.

9. Aßmann, J.; Crihan, D.; Knapp, M.; Lundgren, E.; Löffler, E.; Muhler, M.; Narkhede, V.; Over, H.; Schmid, M.; Seitsonen, A. P.; Varga, P., Understanding the Structural Deactivation of Ruthenium Catalysts on an Atomic Scale under both Oxidizing and Reducing Conditions. *Angew. Chem. Int. Ed.* **2005,** *44* (6), 917-920.

10. Böttcher, A.; Starke, U.; Conrad, H.; Blume, R.; Niehus, H.; Gregoratti, L.; Kaulich, B.; Barinov, A.; Kiskinova, M., Spectral and spatial anisotropy of the oxide growth on Ru(0001). *J. Chem. Phys.* **2002,** *117*, 8104-8109.

11. Chen, M. S.; Cai, Y.; Yan, Z.; Gath, K. K.; Axnanda, S.; Goodman, D. W., Highly active surfaces for CO oxidation on Rh, Pd, and Pt. *Surf. Sci.* **2007,** *601* (23), 5326-5331.

12. Lee, H. I.; White, J. M., Carbon monoxide oxidation over Ru(001). *J. Catal.* **1980,** *63* (1), 261-264.

13. Over, H.; Muhler, M., Catalytic CO oxidation over ruthenium—bridging the pressure gap. *Prog. Surf. Sci.* **2003,** *72* (1–4), 3-17.

14. Reuter, K.; Scheffler, M., Composition, structure, and stability of RuO_2(110) as a function of oxygen pressure. *Phys. Rev. B* **2001,** *65* (3), 035406.

15. Gao, F.; Wang, Y.; Cai, Y.; Goodman, D. W., CO oxidation over Ru(0001) at near-atmospheric pressures: From chemisorbed oxygen to RuO_2. *Surf. Sci.* **2009,** *603* (8), 1126-1134.

16. Rieger, M.; Rogal, J.; Reuter, K., Effect of Surface Nanostructure on Temperature Programmed Reaction Spectroscopy: First-Principles Kinetic Monte Carlo Simulations of CO Oxidation at RuO_2(110). *Phys. Rev. Lett.* **2008,** *100* (1), 016105.

17. Reuter, K.; Stampfl, C.; Verónica Ganduglia-Pirovano, M.; Scheffler, M., Atomistic description of oxide formation on metal surfaces: the example of ruthenium. *Chem. Phys. Lett.* **2002,** *352* (5–6), 311-317.

18. Reuter, K.; Scheffler, M., First-principles kinetic Monte Carlo simulations for heterogeneous catalysis: Application to the CO oxidation at RuO_2(110). *Phys. Rev. B* **2006,** *73* (4), 045433.

19. Vogel, W.; Alonso-Vante, N., Oxygen and carbon monoxide interaction on novel clusters like ruthenium: a WAXS study. *J. Catal.* **2005,** *232* (2), 395-401.

20. Wakita, H.; Ukai, K.; Takeguchi, T.; Ueda, W., Mechanistic Investigation of Deactivation of Ru/Al_2O_3 Catalyst for Preferential CO Oxidation in the Presence of NH_3. *J. Phys. Chem. C* **2007,** *111* (5), 2205-2211.

21. Kiss, J. T.; Gonzalez, R. D., Catalytic oxidation of carbon monoxide over ruthenium/silicon dioxide: an in situ infrared and kinetic study. *J. Phys. Chem.* **1984,** *88* (5), 892-897.

22. Rosenthal, D.; Girgsdies, F.; Timpe, O.; Blume, R.; Weinberg, G.; Teschner, D.; Schlögl, R., On the CO-Oxidation over Oxygenated Ruthenium. *Zeitschrift für Physikalische Chemie*, **2009**, *223*, 183.

23. Assmann, J.; Narkhede, V.; Khodeir, L.; Löffler, E.; Hinrichsen, O.; Birkner, A.; Over, H.; Muhler, M., On the Nature of the Active State of Supported Ruthenium Catalysts Used for the Oxidation of Carbon Monoxide: Steady-State and Transient Kinetics Combined with in Situ Infrared Spectroscopy. *J. Phys. Chem. B* **2004,** *108* (38), 14634-14642.

24. Knapp, M.; Seitsonen, A. P.; Kim, Y. D.; Over, H., Catalytic Activity of the RuO_2(100) Surface in the Oxidation of CO. *J. Phys. Chem. B* **2004,** *108* (38), 14392-14397.

25. Narkhede, V.; Aßmann, J.; Muhler, M., Structure-Activity Correlations for the Oxidation of CO over Polycrystalline RuO_2 Powder Derived from Steady-State and Transient Kinetic Experiments. *Zeitschrift für Physikalische Chemie*, **2005**, *219*, 979-995.

26. Thomas, L. H., The calculation of atomic fields. *Math. Proc. Camb. Philos. Soc.* **1927,** *23* (05), 542-548.

27. Fermi, E., Über die magnetischen Momente der Atomkerne. *Z. Physik* **1930,** *60* (5-6), 320-333.

28. Fermi, E.; Segrè, E., Zur Theorie der Hyperfeinstruktur. *Z. Physik* **1933,** *82* (11-12), 729-749.

29. Langreth, D. C.; Perdew, J. P., Theory of nonuniform electronic systems. I. Analysis of the gradient approximation and a generalization that works. *Phys. Rev. B* **1980,** *21* (12), 5469-5493.

30. Perdew, J. P., Density-functional approximation for the correlation energy of the inhomogeneous electron gas. *Phys. Rev. B* **1986,** *33* (12), 8822-8824.

31. Perdew, J. P., Generalized gradient approximations for exchange and correlation: A look backward and forward. *Physica B: Condensed Matter* **1991,** *172* (1–2), 1-6.

32. Rogal, J.; Reuter, K.; Scheffler, M., Thermodynamic stability of PdO surfaces. *Phys. Rev. B* **2004,** *69* (7), 075421.

33. Reuter, K.; Stampf, C.; Scheffler, M., *Ab Initio* Atomistic Thermodynamics and Statistical Mechanics of Surface Properties and Functions. In *Handbook of Materials Modeling*, Yip, S., Ed. Springer Netherlands: **2005**; pp 149-194.

34. Voter, A., Introduction to the kinetic Monte Carlo Method. In *Radiation Effects in Solids*, Sickafus, K.; Kotomin, E.; Uberuaga, B., Eds. Springer Netherlands: **2007**; Vol. 235, pp 1-23.

35. Reuter, K., First-Principles Kinetic Monte Carlo Simulations for Heterogeneous Catalysis: Concepts, Status, and Frontiers. In *Modeling and Simulation of Heterogeneous Catalytic Reactions*, Wiley-VCH Verlag GmbH & Co. KGaA: **2011**; pp 71-111.

36. Masel, R. I., Chemical Kinetics and Catalysis. *Wiley-Interscience, New York* **2001**.

37. Chorkendorff, I., Niemantsverdriet J. W. , Concepts of Modern Catalysis and Kinetics. *Wiley-VCH, Weinheim* **2003**.

38. Wigner, E. Z., *Phys. Chem. B* **1932,** *19*, 203.

39. Eyring, H., The Activated Complex in Chemical Reactions. *J. Chem. Phys.* **1935,** *3*, 107.

40. Hänggi, P., Talkner, P.; Borkovec, M. , Reaction-rate Theory - 50 Years after Kramers. *Rev. Mod. Phys.* **1990,** *62*, 251-341.

41. Mills, G.; Jónsson, H.; Schenter, G. K., Reversible work transition state theory: application to dissociative adsorption of hydrogen. *Surf. Sci.* **1995,** *324* (2–3), 305-337.

42. Jonsson, H. M., G.; Jacobsen, K. W. , Nudged Elastic Band Method for Finding Minimum Energy Paths of Transitions, in Classical and Quantum Dynamics in Condensed Phase Simulations. *World Scientific* **1998**.

43. Henkelman, G., Uberuaga B .P.; Jonsson, H. , A climbing image nudge elastic band mezhod for finding saddle points and minimum energy paths. *J. Chem. Phys.* **2000,** *113*, 9901.

44. Reuter, K.; Scheffler, M., First-Principles Atomistic Thermodynamics for Oxidation Catalysis: Surface Phase Diagrams and Catalytically Interesting Regions. *Phys. Rev. Lett.* **2003,** *90* (4), 046103.

45. Reuter, K.; Frenkel, D.; Scheffler, M., The Steady State of Heterogeneous Catalysis, Studied by First-Principles Statistical Mechanics. *Phys. Rev. Lett.* **2004,** *93* (11), 116105.

46. Schrödinger, E., An Undulatory Theory of the Mechanics of Atoms and Molecules. *Phys. Rev.* **1926,** *28* (6), 1049-1070.

47. Born, M.; Oppenheimer, R., Zur Quantentheorie der Molekeln. *Annalen der Physik* **1927,** *389* (20), 457-484.

48. Hartree, D. R., The Wave Mechanics of an Atom with a Non-Coulomb Central Field. Part I. Theory and Methods. *Math. Proc. Camb. Philos. Soc.* **1928,** *24* (01), 89-110.

49. Fock, V., Näherungsmethode zur Lösung des quantenmechanischen Mehrkörperproblems. *Z. Physik* **1930,** *61* (1-2), 126-148.

50. Slater, J. C., The Theory of Complex Spectra. *Phys. Rev.* **1929,** *34* (10), 1293-1322.

51. Fermi, E., A statistical method for the determination of some atomic properties and the application of this method to the theory of the periodic system of elements. *Z. Phys.* **1928,** *48*, 73-79.

52. Teller, E., On the Stability of Molecules in the Thomas-Fermi Theory. *Rev. Mod. Phys.* **1962,** *34* (4), 627-631.

53. Bender, M.; Heenen, P. H.; Reinhard, P. G., Self-consistent mean-field models for nuclear structure. *Rev. Mod. Phys.* **2003,** *75* (1), 121-180.

54. Erler, J.; Birge, N.; Kortelainen, M.; Nazarewicz, W.; Olsen, E.; Perhac, A. M.; Stoitsov, M., The limits of the nuclear landscape. *Nature* **2012,** *486* (7404), 509-512.

55. Hohenberg, P.; Kohn, W., Inhomogeneous Electron Gas. *Phys. Rev.* **1964,** *136* (3B), B864-B871.

56. Runge, E.; Gross, E. K. U., Density-Functional Theory for Time-Dependent Systems. *Phys. Rev. Lett.* **1984,** *52* (12), 997-1000.

57. Levy, M., Universal variational functionals of electron densities, first-order density matrices, and natural spin-orbitals and solution of the v-representability problem. *Proc. Natl. Acad. Sci.* **1979,** *76* (12), 6062-6065.

58. Lieb, E. H., Density functionals for coulomb systems. *Int. J. Quantum Chem.* **1983,** *24* (3), 243-277.

59. Kohn, W.; Sham, L. J., Self-Consistent Equations Including Exchange and Correlation Effects. *Phys. Rev.* **1965,** *140* (4A), A1133-A1138.

60. Perdew, J. P.; Schmidt, K., Jacob's ladder of density functional approximations for the exchange-correlation energy. *AIP Conf. Proc.* **2001,** *577* (1), 1-20.

61. Perdew, J. P.; Ruzsinszky, A.; Tao, J.; Staroverov, V. N.; Scuseria, G. E.; Csonka, G. I., Prescription for the design and selection of density functional approximations: More constraint satisfaction with fewer fits. *J. Chem. Phys.* **2005,** *123* (6), 062201.

62. Martin, R. M., Electronic structure: basic theory and practical methods. *Cambridge University Press* **2004**, pp. 7-17.

63. Perdew, J. P.; Burke, K.; Ernzerhof, M., Generalized Gradient Approximation Made Simple. *Phys. Rev. Lett.* **1996,** *77* (18), 3865-3868.

64. Becke, A. D., Density-functional exchange-energy approximation with correct asymptotic behavior. *Phys. Rev. A* **1988,** *38* (6), 3098-3100.

65. Perdew, J. P.; Wang, Y., Accurate and simple analytic representation of the electron-gas correlation energy. *Phys. Rev. B* **1992,** *45* (23), 13244-13249.

66. Hammer, B.; Hansen, L. B.; Nørskov, J. K., Improved adsorption energetics within density-functional theory using revised Perdew-Burke-Ernzerhof functionals. *Phys. Rev. B* **1999,** *59* (11), 7413-7421.

67. Allouti, F.; Manceron, L.; Alikhani, M. E., On the performance of the hybrid TPSS meta-GGA functional to study the singlet open-shell structures: A combined theoretical and experimental investigations of the Ni_2O_2 molecule. *J. Mol. Struc.-THEOCHEM* **2009,** *903* (1–3), 4-10.

68. Scuseria, G. E.; Staroverov, V. N., Progress in the development of exchange-correlation functionals. *Theory and Applications of Computational Chemistry: The First Forty Years.* Elsevier B. V. **2005**, p. 18.

69. Kittel, C; McEuen, P., Introduction to solid state physics. *Wiley, New York* **1986**, p. 19.

70. Ashcroft, N. W.; Mermin, N. D., Solid state physics. *Holt, Rinehart and Winston, New York* **1976**, p. 19.

71. Bloch, F., Über die Quantenmechanik der Elektronen in Kristallgittern. *Z. Physik* **1929,** *52* (7-8), 555-600.

72. Monkhorst, H. J.; Pack, J. D., Special points for Brillouin-zone integrations. *Phys. Rev. B* **1976,** *13* (12), 5188-5192.

73. Press, W.; Teukolsky, S.; Vetterling W.; Flannery, B., Numerical Recipes 3rd Edition: The Art of Scientific Computing. *Cambridge University Press, 3 edition, September* **2007***. ISBN 0521880688.*, p. 14 &30.

74. Frigo, M.; Johnson, S. G., The design and implementation of FFTW3. . *Proceedings of the IEEE, 93(2):216–231,* **2005***. ISSN 0018- 9219.*, p. 14 & 127.

75. Kleinman, L.; Phillips, J. C., Crystal Potential and Energy Bands of Semiconductors. III. Self-Consistent Calculations for Silicon. *Phys. Rev.* **1960,** *118* (5), 1153-1167.

76. Hamann, D. R.; Schlüter, M.; Chiang, C., Norm-Conserving Pseudopotentials. *Phys. Rev. Lett.* **1979,** *43* (20), 1494-1497.

77. Bachelet, G. B.; Hamann, D. R.; Schlüter, M., Pseudopotentials that work: From H to Pu. *Phys. Rev. B* **1982,** *26* (8), 4199-4228.

78. Vanderbilt, D., Soft self-consistent pseudopotentials in a generalized eigenvalue formalism. *Phys. Rev. B* **1990,** *41* (11), 7892-7895.

79. Jónsson, H.; Mills, G.; Jacobsen, K. W., Nudged elastic band method for finding minimum energy paths of transitions. In Classical and Quantum Dynamics in Condensed Phase Simulations. *World Scientific, 385.*

80. Henkelman, G.; Jónsson, H., Improved tangent estimate in the nudged elastic band method for finding minimum energy paths and saddle points. *J. Chem. Phys.* **2000,** *113* (22), 9978-9985.

81. Pratt, L. R., A statistical method for identifying transition states in high dimensional problems. *J. Chem. Phys.* **1986,** *85* (9), 5045-5048.

82. Stull, D. R.; Prophet, H., *JANAF thermochemical tables*. U.S. Dept. of Commerce, National Bureau of Standards: Washington, D.C, **1971**.

83. Reuter, K.; Scheffler, M., Composition and structure of the RuO_2(110) surface in an O_2 and CO environment: Implications for the catalytic formation of CO_2. *Phys. Rev. B* **2003,** *68* (4), 045407.

84. Rogal, J., Reuter, K., *Ab initio* atomistic thermodynamics for surfaces: A primer. In: Experiment, Modeling and Simulation of Gas-Surface Interactions for Reactive Flows in Hypersonic Flights. Educational Notes RTO-EN-AVT-142. *Neuilly-sur-Seine, ISBN 978-92-837-0057-9.* **2007**, *p. 2-1—2-18.*

85. Temel, B.; Meskine, H.; Reuter, K.; Scheffler, M.; Metiu, H., Does phenomenological kinetics provide an adequate description of heterogeneous catalytic reactions? *J. Chem. Phys.* **2007,** *126* (20), 204711.

86. Fichthorn, K. A.; Weinberg, W. H., Theoretical foundations of dynamical Monte Carlo simulations. *J. Chem. Phys.* **1991,** *95* (2), 1090-1096.

87. Hoffmann, M. J.; Matera, S.; Reuter, K., kmos: A lattice kinetic Monte Carlo framework. *Comput. Phys. Commun.* **2014,** *185* (7), 2138-2150.

88. Gai, P. L.; Boyes, E. D.; Helveg, S.; Hansen, P. L.; Giorgio, S.; Henry, C. R., Atomic-Resolution Environmental Transmission Electron Microscopy for Probing Gas–Solid Reactions in Heterogeneous Catalysis. *MRS Bulletin* **2007,** *32* (12), 1044-1050.

89. Topsøe, H., Developments in operando studies and in situ characterization of heterogeneous catalysts. *J. Catal.* **2003,** *216* (1–2), 155-164.

90. Molenbroek, A.; Helveg, S.; Topsøe, H.; Clausen, B., Nano-Particles in Heterogeneous Catalysis. *Top Catal* **2009,** *52* (10), 1303-1311.

91. Buurmans, I. L. C.; Weckhuysen, B. M., Heterogeneities of individual catalyst particles in space and time as monitored by spectroscopy. *Nat. Chem.* **2012,** *4* (11), 873-886.

92. Stampfl, C.; Veronica Ganduglia-Pirovano, M.; Reuter, K.; Scheffler, M., Catalysis and corrosion: the theoretical surface-science context. *Surf. Sci.* **2002,** *500* (1–3), 368-394.

93. Sabbe, M. K.; Reyniers, M.-F.; Reuter, K., First-principles kinetic modeling in heterogeneous catalysis: an industrial perspective on best-practice, gaps and needs. *Catal. Sci. Tech.* **2012,** *2* (10), 2010-2024.

94. Curie, P., Sur la formation des cristaux et sur les constantes capillaires de leurs différentes faces. *Bull. Soc. Mineral. Fr* **1885,** *8*, 145.

95. Raybaud, P.; Digne, M.; Iftimie, R.; Wellens, W.; Euzen, P.; Toulhoat, H., Morphology and Surface Properties of Boehmite (γ-AlOOH): A Density Functional Theory Study. *J. Catal.* **2001,** *201* (2), 236-246.

96. Mittendorfer, F.; Seriani, N.; Dubay, O.; Kresse, G., Morphology of mesoscopic Rh and Pd nanoparticles under oxidizing conditions. *Phys. Rev. B* **2007,** *76* (23), 233413.

97. Nicola, S., Ab initio thermodynamics of lithium oxides: from bulk phases to nanoparticles. *Nanotechnology* **2009,** *20* (44), 445703.

98. Rosenthal, D.; Girgsdies, F.; Timpe, O.; Weinberg, G.; Schlögl, R., Oscillatory behavior in the CO-oxidation over bulk ruthenium dioxide – the effect of the CO/O_2 ratio. *Zeitschrift für Physikalische Chemie* **2011,** *225*, 57-68.

99. Reuter, K., Impact de la pression et de l'état du matériau sur la réactivité : oxydation de CO avec des catalyseurs de "ruthénium". *Oil & Gas Science and Technology - Rev. IFP* **2006,** *61* (4), 471-477.

100. Over, H., Surface Chemistry of Ruthenium Dioxide in Heterogeneous Catalysis and Electrocatalysis: From Fundamental to Applied Research. *Chem. Rev.* **2012,** *112* (6), 3356-3426.

101. Kim, Y. D.; Over, H.; Krabbes, G.; Ertl, G., Identification of RuO_2 as the active phase in CO oxidation on oxygen-rich ruthenium surfaces. *Top Catal* **2000,** *14* (1-4), 95-100.

102. Böttcher, A.; Rogozia, M.; Niehus, H.; Over, H.; Ertl, G., Transient Experiments on CO_2 Formation by the CO Oxidation Reaction over Oxygen-Rich Ru(0001) Surfaces. *J. Phys. Chem. B* **1999,** *103* (30), 6267-6271.

103. Aßmann, J.; Crihan, D.; Knapp, M.; Lundgren, E.; Löffler, E.; Muhler, M.; Narkhede, V.; Over, H.; Schmid, M.; Seitsonen, A. P.; Varga, P., Understanding the

Structural Deactivation of Ruthenium Catalysts on an Atomic Scale under both Oxidizing and Reducing Conditions. *Angew. Chem.* **2005,** *117* (6), 939-942.

104. Clark Stewart, J.; Segall Matthew, D.; Pickard Chris, J.; Hasnip Phil, J.; Probert Matt, I. J.; Refson, K.; Payne Mike, C., First principles methods using CASTEP. *Zeitschrift für Kristallographie*, **2005**, *220*, 567.

105. Kaminsky, W., WinXMorph: a computer program to draw crystal morphology, growth sectors and cross sections with export files in VRML V2.0 utf8-virtual reality format. *J. Appl. Crystallogr.* **2005,** *38* (3), 566-567.

106. Kaminsky, W., From CIF to virtual morphology using the WinXMorph program. *J. Appl. Crystallogr.* **2007,** *40* (2), 382-385.

107. Henrich, V. E.; Cox, P. A., The Surface Science of Metal Oxides. *Cambridge University Press* **1994**.

108. Noguera, C., Physics and Chemistry at Oxide Surfaces. *Cambridge University Press* **1996**.

109. López, N.; Gómez-Segura, J.; Marín, R. P.; Pérez-Ramírez, J., Mechanism of HCl oxidation (Deacon process) over RuO_2. *J. Catal.* **2008,** *255* (1), 29-39.

110. Wulff, G., On the Question of Speed of Growth and Dissolution of Crystal Surfaces. *Z. Kristallogr* **1901,** *34*, 449-530.

111. Huang, Y. S.; Park, H. L.; Pollak, F. H., Growth and characterization of RuO_2 single crystals. *Mater. Res. Bull.* **1982,** *17* (10), 1305-1312.

112. Shafer, M. W.; Figat, R. A.; Olson, B.; LaPlaca, S. J.; Angilello, J., Preparation and Characterization of Ruthenium Dioxide Crystals. *J. Elechem. So.* **1979,** *126* (9), 1625-1628.

113. Boudart, M., Catalysis by Supported Metals. *Adv. Catal.* **1969,** *20*, 153-166.

114. Somorjai, G. A.; Carrazza, J., Structure sensitivity of catalytic reactions. *Ind. Eng. Chem. Fundam.* **1986,** *25* (1), 63-69.

115. Marsh, A. L.; Ribeiro, F. H.; Somorjai, G. A., Single Crystal Surfaces. In: Handbook of Heterogeneous Catalysis. **2008**, pp. 1259–1276.

116. Ertl, G.; Knözinger, H.; Schüth, F., *(Eds.). Wiley: Hoboken, NJ,* **2008**.

117. Wang, T.; Jelic, J.; Rosenthal, D.; Reuter, K., Exploring Pretreatment–Morphology Relationships: *Ab Initio* Wulff Construction for RuO_2 Nanoparticles under Oxidising Conditions. *ChemCatChem.* **2013,** *5* (11), 3398-3403.

118. Matera, S.; Meskine, H.; Reuter, K., Adlayer inhomogeneity without lateral interactions: Rationalizing correlation effects in CO oxidation at RuO_2(110) with first-principles kinetic Monte Carlo. *J. Chem. Phys.* **2011,** *134* (6), 064713.

119. Reuter, K., First-Principles kinetic Monte Carlo Simulations for Heterogeneous Catalysis: Concepts, Status, and Frontiers. In: Modelling and Simulation of Heterogeneous Catalytic Reactions: From the Molecular Process to the Technical System. *Deutschmann, O. (Ed.), Wiley-VCH: Weinheim, ISBN-10: 3-527-32120-9.* **2011***,* pp. 71-112.

120. Norskov, J. K.; Bligaard, T.; Hvolbaek, B.; Abild-Pedersen, F.; Chorkendorff, I.; Christensen, C. H., The nature of the active site in heterogeneous metal catalysis. *Chem. Soc. Rev.* **2008,** *37* (10), 2163-2171.

121. Van Santen, R. A., Complementary Structure Sensitive and Insensitive Catalytic Relationships. *Accounts Chem. Res.* **2009,** *42* (1), 57-66.

122. Cramer, C. J., Essentials of Computational Chemistry: Theories and Models. *WILEY* **2002**.

123. Henkelman, G.; Uberuaga, B. P.; Jónsson, H., A climbing image nudged elastic band method for finding saddle points and minimum energy paths. *J. Chem. Phys.* **2000,** *113* (22), 9901-9904.

124. Bahn, S. R.; Jacobsen, K. W., An object-oriented scripting interface to a legacy electronic structure code. *Computing in Science & Engineering* **2002,** *4* (3), 56-66.

125. Zhang, Y.; Blum, V.; Reuter, K., Accuracy of first-principles lateral interactions: Oxygen at Pd(100). *Phys. Rev. B* **2007,** *75* (23), 235406.

126. Rogal, J.; Reuter, K.; Scheffler, M., CO oxidation on Pd(100) at technologically relevant pressure conditions: First-principles kinetic Monte Carlo study. *Phys. Rev. B* **2008,** *77* (15), 155410.

127. Hoffmann, M.; Reuter, K., CO Oxidation on Pd(100) Versus PdO(101)-($\sqrt{5}\times\sqrt{5}$) R27°: First-Principles Kinetic Phase Diagrams and Bistability Conditions. *Top Catal* **2014,** *57* (1-4), 159-170.

128. Hoffmann, M. J.; Scheffler, M.; Reuter, K., Multi-lattice Kinetic Monte Carlo Simulations from First Principles: Reduction of the Pd(100) Surface Oxide by CO. *ACS Catalysis* **2015,** *5* (2), 1199-1209.

129. Hirvi, J. T.; Kinnunen, T.-J. J.; Suvanto, M.; Pakkanen, T. A.; Nørskov, J. K., CO oxidation on PdO surfaces. *J. Chem. Phys.* **2010,** *133* (8), 084704.

130. Wang, J.; Fan, C. Y.; Sun, Q.; Reuter, K.; Jacobi, K.; Scheffler, M.; Ertl, G., Surface Coordination Chemistry: Dihydrogen versus Hydride Complexes on RuO_2(110). *Angew. Chem. Int. Ed.* **2003,** *42* (19), 2151-2154.

131. Reuter, K.; Scheffler, M., Surface core-level shifts at an oxygen-rich Ru surface: O/Ru(0001) vs. RuO_2(110). *Surf. Sci.* **2001,** *490* (1–2), 20-28.

132. Seitsonen, A. P.; Kim, Y. D.; Knapp, M.; Wendt, S.; Over, H., CO adsorption on the reduced RuO_2(110) surface: Energetics and structure. *Phys. Rev. B* **2001,** *65* (3), 035413.

133. Joo, S. H.; Park, J. Y.; Renzas, J. R.; Butcher, D. R.; Huang, W.; Somorjai, G. A., Size Effect of Ruthenium Nanoparticles in Catalytic Carbon Monoxide Oxidation. *Nano Lett.* **2010,** *10* (7), 2709-2713.

List of publications

1. Wang, T.; Jelic, J.; Rosenthal, D.; Reuter, K., Exploring Pretreatment–Morphology Relationships: *Ab Initio* Wulff Construction for RuO_2 Nanoparticles under Oxidising Conditions. *ChemCatChem* **2013,** *5*, 3398.
2. Wang, T.; Reuter, K. Structure Sensitivity in Oxide Catalysis: First-Principles kinetic Monte Carlo Simulations for CO oxidation at RuO_2 (111). (Submitted to J. Chem. Phys.)

List of abbreviations

1p-kMC	First-principles kinetic Monte Carlo
CI-NEB	Climbing Images Nudged Elastic Band
DFT	Density Functional Theory
GGA	Generalized Gradient Approximation
HK	Hohenberg–Kohn
kMC	kinetic Monte Carlo
LDA	Local Density Approach
MEP	Minimum Energy Path
NEB	Nudged Elastic Band
PBC	Periodic Boundary Conditions
PBE	Perdew–Burke–Ernzerhof
PES	Potential Energy Surface
PM-IRAS	Polarization Modulation Infrared Reflection Absorption Spectroscopy
RuO_2	Ruthenium dioxide
RuO_X	Ruthenium oxides
TDDFT	Time-Dependent Density Functional Theory
TOF	TurnOver Frequency
UHV	Ultra-High Vacuum
XPS	X-ray Photoelectron Spectroscopy
XRD	X-Ray Diffraction

Acknowledgements

The completion of this work would not be possible without the support and help from many people.

First of all, I would like to thank **Prof. Dr. Karsten Reuter** for giving me the opportunity to perform my doctoral research in our group. This decision has doubtlessly helped me in several aspects of my life. Thank you for your guidance and advice that help me to overcome the obstacles and always keep me on track. Thank you for generously sharing your expertise and experience with me to support me growing as a research scientist. Thank you for providing me so many chances to attend various trainings and conferences that enhance my presentation skills, broaden my research horizons and develop a continuing and wide-ranging research partnership. And thank you for your advices on my career that encourage me to fully explore my potentials.

I would like to express my great appreciation to every single member of our group who makes my PhD time full of joy. I enjoy both working with you and having fun together with you in numerous group activities. Special thanks go to **Dr. Jelena Jelic** who supervised me on my first subject of PhD subject. Thank you for your support and friendly communications that gave me a good start with my PhD. I would also like to thank our 'Catalysis subgroup' formed with **Dr. Farnaz Sotoodeh, Dr. Mie Andersen, Dr. Ary Ferreira, Dr. Craig Plaisance, Juan Manuel Lorenzi, Zhen Yao** and **Claudia D'Amario**. It is so great to change ideas and opinions, share solutions and experiences, and always have fruitful discussions with you guys. I gratefully acknowledge **Dr. Max Hoffmann, Dr. Sebastian Matera, Dr. Reinhard Maurer, Dr. Dennis Palagin, Konstantin Krautgasser** and **Dr. Saskia Stegmaier** for your help with my research, for numerous scientific discussions, and for making pleasant cooperations. Furthermore, I would like to thank our IT professionals **Dr. Christoph Scheurer, Dr. Max Hoffmann, Christoph Schober, Georg Michelitsch, Juan Manuel Lorenzi,** and **Stefan Ringe** for your technical support and our secretary **Ruth Mösch** for making things work smoothly.

I also would like to express many thanks to my teaching partners **Peter Kämmerer, Dr. Alexander Ogrodnik,** and **Michele Piana** in Physical Chemistry lab course. Thank you

for sharing me with teaching skills and making the teaching meaningful and active. Also special thanks for all my lovely students, for your positive feedback and your support.

I would like to thank the **China Scholarship Council** for a scholarship and **TUM Graduate School** for providing numerous soft-skill courses and for financial support on conferences and workshops. Furthermore, I gratefully acknowledge generous access to computing time at the **Leibniz Supercomputing Centre** under grant ‘pr86de’.

I am deeply thankful to my family for your love, support, and sacrifices. Without you, this thesis would never have been written. Further thanks to all my friends who bring me so much happiness in my life during my doctorate.

With these two lines, I would also like to thank all the people that helped in any way during this time and were not mentioned in the previous lines.